

# A Comparative Study of Thermo-Mechanical Fatigue Performance of Different Grades of SiMo Nodular Cast Iron

By

Siddharth Shankar

in partial fulfilment of the requirements for the degree of

**Master of Science**

in Materials Science and Engineering

at the Delft University of Technology,

to be defended publicly on Thursday September 27<sup>th</sup>, 2018 at 2:00 PM.

Thesis committee: Prof. dr. ir. L.A.I Kestens

Prof. dr. ir. Roumen H. Petrov

Dr. ir. A.C. Riemsdag, TU Delft

Ir. A. Kalra, DAF Trucks N.V.

# Contents

1. Introduction .....	5
1.1. Research Goals .....	6
1.2. Thesis Structure .....	7
2. Background Study .....	8
2.1. Introduction to Cast Iron .....	8
2.2. Introduction to High Silicon – Molybdenum Cast Iron.....	8
2.3. Solidification of High Silicon – Molybdenum Cast Iron .....	9
2.4. Graphitizers.....	10
Silicon .....	11
Phosphorous.....	11
Sulfur.....	11
2.5. Spheroidizers .....	11
Magnesium .....	12
2.6. Microstructure of High Silicon – Molybdenum Cast Iron.....	12
Carbide phase.....	13
Dimensional Stability.....	14
2.7. Heat-treatment of Silicon-Molybdenum Ferritic Cast Iron.....	14
2.8. Mechanical Properties of Silicon – Molybdenum Cast Iron .....	16
2.9. Thermo-mechanical Fatigue ( <i>TMF</i> ) Concepts.....	20
2.10. Thermal and Mechanical Strains in <i>TMF</i> .....	20
2.11. Out-of-phase <i>TMF</i> .....	20
2.12. Holding time in <i>TMF</i> .....	21
2.13. Prediction of <i>TMF</i> lifetime .....	22
2.14. Thermo-mechanical Fatigue in Silicon – Molybdenum Cast Irons .....	22
3. Experimental Approach.....	26
3.1. <i>TMF</i> Test Specimen and Material .....	26
3.2. Experimental Set-up.....	28
3.3. <i>TMF</i> Test series Performed.....	30

TMF Test Series Benchmark Ranking .....	32
TMF Test Series with $T_{\min}$ 150 °C .....	33
TMF Test Series effect of $t_{\text{hold}}$ .....	33
3.4. Coefficient of Thermal Expansion (CTE) .....	34
3.5. TMF Test Termination Criterion .....	35
3.6. Paris Lifetime Calculations .....	36
3.7. Material Characterization .....	37
3.8. Optical Microscopy .....	37
3.9. Scanning Electron Microscopy .....	38
3.10. Vickers Hardness Testing .....	38
4. Results and discussion .....	39
4.1. <i>TMF</i> Results – Lifetimes and Stress-Strain development .....	39
TMF Test Series Benchmark Ranking .....	39
TMF Test Series with $T_{\min}$ 150 °C .....	42
TMF Test Series effect of $t_{\text{hold}}$ .....	43
4.2. Effect of Notching in SiMoNi – Fracture Toughness vs Fatigue .....	47
4.3. Paris Lifetime Calculations .....	48
4.4. Material Characterization .....	50
5. Conclusions and Recommendations for Future Research .....	55
5.1. Conclusions .....	55
5.2. Recommendations .....	55
6. Appendices .....	57
A. Results of the <i>TMF</i> Test Series .....	57
B. Previously performed <i>TMF</i> tests on SiMoNi Nodular cast iron .....	59
C. Measuring the Compliance of a Circumferentially Cracked dog-bone Specimen .....	60
D. MATLAB scripts .....	62
7. Bibliography .....	63

# Abstract

This thesis is a comparative study of the Thermo-Mechanical Fatigue (*TMF*) performance of different grades of SiMo nodular cast iron for heavy-duty diesel engine exhaust gas manifold applications. The *TMF* performance of the current SiMo variant used to manufacture exhaust manifolds - SiMo 5.10 (C-3.25Si-4.45Mo-0.76), is compared with that of the variants SiMo 4.05 (C-3.22Si-4.66Mo-0.56) and SiMoNi (C-3.3Si-4.5Mo-1Ni-1.3) by performing three out-of-phase (OP) *TMF* test series under partial constraint conditions. A benchmark *TMF* test series in the temperature range: 50 °C to 550 °C with a hold time of 30 s at 550 °C showed that SiMo 5.10 had relatively better performance due to development of lower mechanical crack driving forces compared to other variants. However, a long holding time of 600 s at 550 °C saw a larger decrease of average *TMF* lifetimes for SiMo 5.10 than that of SiMo 4.05 despite similar crack driving forces. An investigation of the stress relaxation during *TMF* of the two variants showed that the SiMo 4.05 performs better during long hold time due to better stress relaxation properties. The SiMoNi variant which is very brittle at low temperatures was found to fail by a fracture by overloading mechanism taking over quite early in the fatigue cycle; which is confirmed by examination of the fracture surfaces and numerical estimations. This also explained the low lifetimes and scatter in previously performed *TMF* tests under total constraint conditions. The *TMF* test series performed in the temperature range: 150 °C to 550 °C with a hold time of 30 s at 550 °C found that a heat-treatment seemed to reduce the *TMF* performance of the SiMo 5.10 variant. Metallographic investigations and hardness measurements of as-cast and heat-treated materials revealed that the distribution of the Mo-rich phase from the grain boundary regions into the matrix due to the annealing heat-treatment seems to affect the *TMF* performance.

# 1. Introduction

Recently, the emission standards for heavy-duty diesel engines have become increasingly stringent to limit the environmental effects of exhaust gases. By improving the fuel efficiency the emissions are reduced [1]. This leads to increased exhaust gas temperatures which causes higher operating demands on exhaust manifolds. In order to cope with this DAF Trucks N.V. is evaluating new materials for manufacturing exhaust manifolds.

During operation, exhaust manifolds are submitted to internal hot gas pressure and a varying wide temperature range. They are subject to severe thermal and mechanical loading cycles which become prominent during engine start-up and stop [2] [3]. In fully loaded conditions, temperatures in the exhaust manifold reach up to 550 °C and during unloaded conditions the temperature reaches 50 °C.

This temperature cycling in complex engine components causes thermal gradients which result in thermal expansion mismatch. Since the exhaust manifold is clamped on to the engine body and constrained by surrounding material at different relative temperatures, thermal strains developing in the component turn to mechanical strains. Such repeated thermal cycles cause out-of-phase loading, i.e. compressive strains are developed during the heating cycle whereas tensile strains are developed during the cooling cycle.

This combination of cyclic thermal and mechanical strains causes Thermo-Mechanical Fatigue (TMF). After a number of cycles, crack initiation and propagation occur on localized regions of the exhaust manifold due to inelastic strains. These cracks affect the durability of the exhaust manifold and eventually may lead to complete failure of the component. Therefore, materials with good high temperature mechanical and physical properties are required for manufacturing exhaust manifolds.

Currently, the exhaust manifolds of DAF engines are made with the material SiMo 5.10 which conforms to a nodular graphitic SiMo cast iron variant with a ferritic matrix alloyed with 4.45%<sup>a</sup> silicon and 0.76% molybdenum. The material is selected for its excellent mechanical properties, high temperature properties and oxidation resistance. The high Si content increases the temperature up to which ferrite is stable, hence improving the microstructural stability of the ferritic matrix at elevated temperatures [2]. The Mo content increases the strength of the material at high temperature due to formation of

---

<sup>a</sup> weight percentage

eutectic carbides at grain boundaries [3]. However, the difference in the coefficients of thermal expansion of the ferritic matrix and the graphite particles also leads to the development of mechanical strains on a microscale [4].

The current project presented here is done in collaboration between DAF trucks N.V. and the Delft University of Technology. The main aim of this research is to investigate and compare the *TMF* performance of different SiMo cast iron variants which can serve as alternatives for the current material used to manufacture exhaust manifolds – SiMo 5.10.

Georg Fischer Automotive, a casting solutions provider for DAF trucks has promoted SiMoNi [5], a SiMo variant which is alloyed with 1-1.3% Nickel. It is reported [6] to have a lower coefficient-of thermal expansion and a better scaling resistance relative to SiMo 5.10. FVV published a report [7] that investigated the variant SiMo 4.05 in which, the reduction of Molybdenum content to 0.56% relative to SiMo 5.10 resulted in relatively better stress relaxation properties and also better fracture strain. It is well known that stress relaxation at high temperature is detrimental to fatigue life [8]. Therefore, the effect of stress relaxation properties of SiMo 5.10 and SiMo 4.05 on their thermo-mechanical fatigue performance is investigated.

Currently, the exhaust manifolds manufactured using the SiMo 5.10 material undergo an expensive and time consuming heat-treatment process. Monotonic tensile tests performed at different temperatures show that heat-treated SiMo5.10 material has better mechanical properties at room temperature relative to its non-heat-treated treated equivalent. However, at temperatures above 150 °C, they have comparable properties. Since the temperatures in exhaust manifolds do not reach room temperature during service the advantages of heat-treatment for *TMF* performance are unclear; hence investigated.

The above mentioned investigations are performed by designing three sets of *TMF* tests that are executed in the Mechanical Behavior Laboratory at TU Delft. This is achieved by designing smaller scale material tests which closely mimic the truck operating conditions during basic Hot-Cold (HC) and Heavy Duty Load Cycle (HDLC) engine tests. By conducting *TMF* tests and changing the parameters of compressive hold time and lower cycle temperature, the effect of stress relaxation and heat-treatment, respectively on *TMF* lifetime is better understood.

## **1.1. Research Goals**

To make clear the investigations performed and discussion that follows, the main research objectives of this thesis project are summarized below:

- To compare and rank the *TMF* performance of SiMo 5.10, SiMo 4.05 and SiMoNi materials by investigating the effect of elevated temperatures and thermal cycling during short hold time *TMF* tests and identifying the damage mechanism. Previously performed *TMF* tests on SiMoNi showed scatter and inconsistencies in lifetime. An attempt is made to address this by studying the effect of notching and investigating the fatigue crack growth during *TMF*.
- To study the effect of heat-treatment on *TMF* performance of SiMo 5.10 by characterizing the microstructural changes due to heat-treatment and studying the effect of lower cycle temperature.
- To evaluate the effect of holding time at high temperature on the *TMF* performance of SiMo 5.10 and SiMo 4.05 by comparing their stress relaxation properties.

## 1.2. Thesis Structure

The second chapter – Background Study – is an overview of reported literature on SiMo cast irons. This chapter provides a basic introduction to the family of cast irons and also an introduction to SiMo ductile cast irons. The solidification of SiMo cast iron is explained along with the role of different elements and their effect on microstructure and mechanical properties. Also, a comprehensive review on previously performed work on heat-treatment, high temperature behavior and thermomechanical fatigue testing of SiMo cast irons is provided.

In the third chapter – Experimental Approach, first, a brief introduction to alloy compositions of the materials tested as well as specimen geometry and specimen preparation is given. This chapter also deals with the test setup and the procedures undertaken to perform *TMF* testing on the specimens. Methods to characterize the materials are explained.

The fourth chapter presents and interprets the results obtained from the *TMF* tests and material characterization through procedures mentioned in the third chapter. The high temperature mechanical behavior of the materials is explained through analyzing the (mechanical) hysteresis loops that develop during the *TMF* tests. The numerical estimation of *TMF* lifetimes is calculated using previously derived parameters to check for validity of the tests performed. An attempt is made to explain the results obtained by putting forth suitable hypotheses through a discussion of the results.

Finally, a fifth chapter presents the main conclusions of the investigations performed and also provides recommendations and scope for future projects along similar lines of testing *TMF* phenomenon in SiMo ductile cast irons.

## 2. Background Study

### 2.1. Introduction to Cast Iron

Cast irons are alloys comprising iron with carbon as the main alloying elements. While steels usually contain less than one percent of carbon, cast irons contain more than two percent carbon. As the name suggests, cast irons are casted from molten iron. Since two percent is the maximum carbon content at which iron can solidify as a single phase alloy, cast irons solidify as heterogeneous alloys i.e. they have more than one constituent in their microstructure [9].

In addition to carbon, cast irons are alloyed with silicon. While white cast irons contain less than 0.8% Si, graphitic cast irons are alloyed with 1-3% Si. The high carbon and silicon content makes graphitic cast irons excellent casting alloys. The increased carbon content reduces the viscosity and melting point enabling molten iron to flow better than molten steel. This allows the production of complex castings. Besides process advantages, the formation of a low density graphite phase during solidification is an added advantage. This graphite phase reduces the shrinkage defects resulting from volume change when the metal transforms from liquid to solid. The microstructure of graphitic cast iron contains two primary components – the graphite phase and a surrounding matrix. Based on the shape and form of the graphite phase, they are classified into four types. They are classified into ductile or nodular cast iron, malleable cast iron, compacted graphite cast iron and gray or lamellar cast iron [9] [10].

Ductile cast iron and Gray cast iron are the most commonly used cast irons to manufacture exhaust manifolds. In gray cast irons, the graphite phase is present in form of separate two-dimensional flakes which are interconnected within each eutectic cell, whereas in ductile cast irons the graphite phase is present as nodules or spheres. The matrix of gray and ductile cast irons can be ferritic, pearlitic, bainitic or even austenitic based on the alloying and cooling rates during solidification. The different graphite phase morphologies along with the matrix constitute the microstructure of the cast iron. Each microstructure gives the cast iron its distinct mechanical and thermal properties. Compared to gray irons, ductile cast irons show a better toughness, less heat conduction and a better resistance to crack growth [1].

### 2.2. Introduction to High Silicon – Molybdenum Cast Iron

High alloy irons are an important group of cast irons which are designed for a specific purpose and that have alloy contents that exceed three percent. They can only be produced by foundries that are specifically equipped to produce high alloyed compositions. Ductile irons containing high silicon content were invented by the British

Cast Iron and Research Association (BCIRA). High silicon ductile irons contain 14.2-14.7% silicon and are used widely for their excellent corrosion resistance [9].

For elevated temperature applications, intermediate silicon irons alloyed with molybdenum and consisting of a stable ferritic microstructure and nodular graphite morphology are used. SiMo (Silicon Molybdenum) or HiSiMo (High Silicon Molybdenum) cast iron is a nodular or ductile cast iron containing 4-6% Si and 0.5-2% Mo [2]. By varying the silicon and molybdenum content, many types of SiMo cast iron has been produced. Many advantages of increased additions of Silicon and Molybdenum such as oxidation resistance, machinability and favorable high temperature mechanical properties and creep properties have been reported [2] [3] [11] [12]. However, an increase of the molybdenum content above 1% is often to be avoided as molybdenum carbides provide crack initiation sites during deformation as the dislocations tend to pile up at the carbide-matrix interface [12].

### **2.3. Solidification of High Silicon – Molybdenum Cast Iron**

SiMo ductile cast iron is a quaternary Fe-C-Si-Mo alloy [13]. In cooling from an inoculated liquid state to form solid SiMo ductile cast iron, many elements and conditions play a role in obtaining the solidified material with desired microstructure and properties. The process of inoculation is explained later in this section. By studying the solidification process, the effect of the elements and cooling conditions are better understood.

Cooling from the liquid state under equilibrium slow cooling rate conditions, the graphite phase first solidifies at the liquidus temperature in a hypereutectic iron with Carbon Equivalent (CE) = 4.6% as seen in figure 2.1. The carbon equivalent given by equation 2.1 is used to understand the effect of carbon and alloying elements on casting behavior by determining the nature of the iron as hypoeutectic, hypereutectic or eutectic. An optimum CE value around 4.7% is required to avoid casting defects [13] [14]. The first solidified graphite phase grows by depleting the liquid iron of carbon. Austenite nucleates in the carbon-depleted areas around the graphite particles, thereby forming a shell around them. The controlling mechanism of graphite nodule growth is the transport of carbon atoms through the austenitic shells, as the graphite particles do not have direct contact with the liquid iron. This process continues until the temperature reaches the eutectic transformation range.

$$CE = \%C + \frac{1}{3}(\%Si + \%P) \quad (2.1)$$

After complete solidification, as the solubility of carbon in austenite decreases with decreasing temperature, carbon diffuses towards the graphite nodules. At the eutectoid temperature, austenite transforms into ferrite by almost completely expelling carbon, as

its solubility in ferrite is less than in austenite. This results in an equilibrium microstructure of a ferritic matrix with nodular graphite particles [15].

## 2.4. Graphitizers

The elements that promote crystallization of graphite in the solidification process are called graphitizers. Silicon, carbon and phosphorus are graphitizers and they have a combined effect on graphite formation. This is estimated by the carbon equivalent equation 2.1 [13] [15].

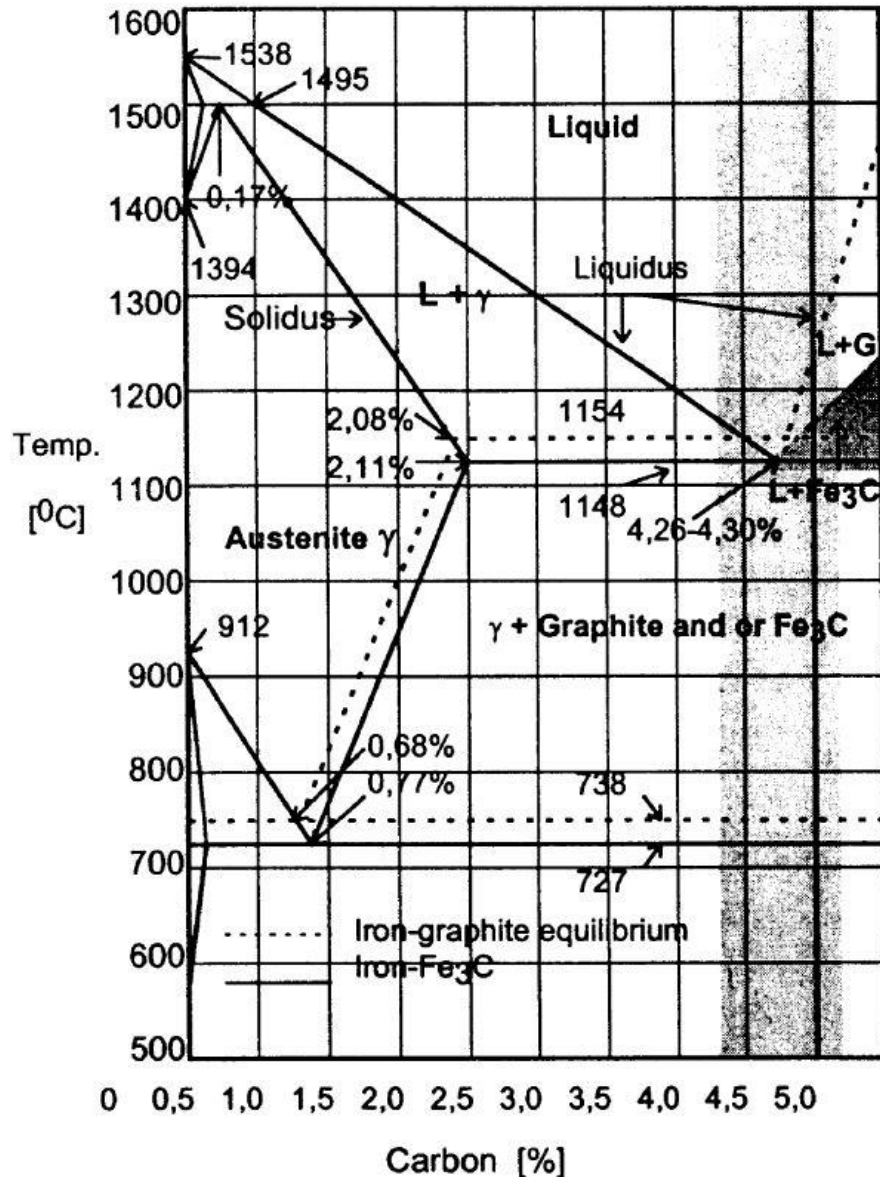


Figure 2.1 Schematic Fe-C binary phase diagram [15]

### **Silicon**

Si favors the graphitic-austenitic system by decreasing the solubility of carbon in austenite and increasing the stable eutectic and eutectoid temperature. This increases the operational temperature range of the material. Si being present in solid solution in ferrite increases the hardness, ultimate tensile strength and yield strength of the matrix but reduces its elongation at fracture and toughness at fracture [9] [16].

Inoculation is the process of increasing graphite nucleation sites by adding inoculant materials to the liquid iron before casting. Si is used as an inoculant in the form of ferrosilicon alloys which promotes precipitation of hexagonal silicate phase of the form  $XOSiO_2$  (where X denotes Ca, Sr or Ba). The basal planes of these hexagonal crystals are favorable sites for graphite nucleation since it allows the formation of coherent or semicoherent low-energy interfaces between the nucleus and graphite. Thus, Si raises the number of nucleation sites and the number of nodules. This reduces the carbon diffusion path during the eutectoid transformation and increases the amount of ferrite in the structure [15].

### **Phosphorous**

Phosphorous is often considered a damaging element in ductile cast irons [15]. Although it promotes the formation of graphite, it also promotes the formation of pearlite. Above certain concentrations, P reacts with Fe to form steadite ( $Fe_3P$ ). Steadite precipitates as a eutectic in the grain boundaries thereby causing embrittlement of the casting. In the concentration range 0.04-0.07% a slight reduction of the impact properties is observed. Increase in P concentration above 0.08% reduces the toughness and increases the ductile-to-brittle transition temperature. The recommended maximum concentration of P is 0.03% for as cast ferritic grades [15] [17].

### **Sulfur**

Sulphur is an active surface element which is absorbed by the graphite phase and hence affects the growth mechanism. This affects the graphite growth mechanisms as it favors the formation of flake graphite instead of nodules. The sulfur content is critical – lesser than 0.010% would lead to very few graphite nodules whereas more than 0.015% would cause a flake like morphology [15].

## **2.5. Spheroidizers**

Elements that determine the shape of the graphite particles are called spheroidizers. The fatigue properties of SiMo ductile cast iron depend on the degree of spheroidization [18].

## Magnesium

Magnesium is the most important and commonly used spheroidizing element. It is widely used because of its low cost and applicability to irons over a wide range of carbon equivalent values and casting sections. It is usually used in ranges from 0.02% to 0.08%. The overall effectiveness in forming the microstructure depends on the sulfur and oxygen content [15].

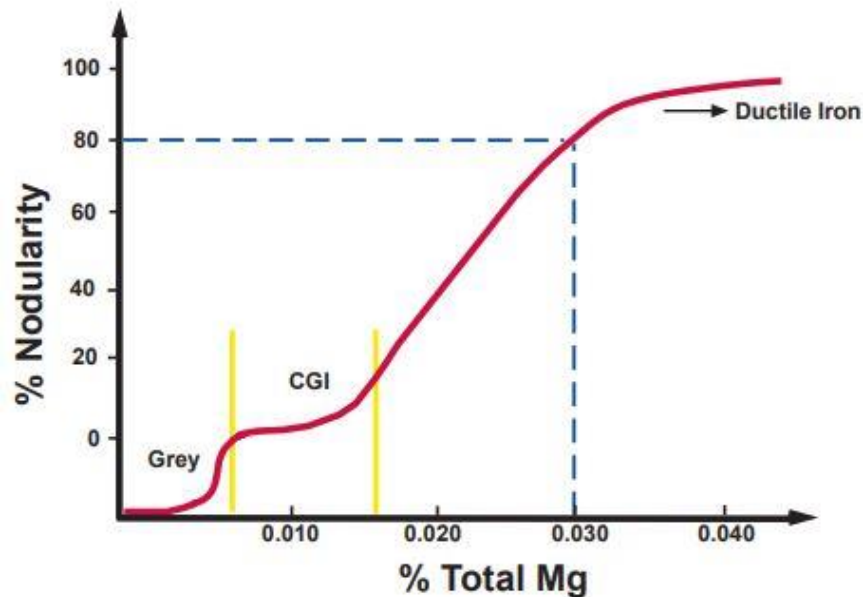


Figure 2.2 Effect of Mg on final shape of graphite [19]

It can be seen from figure 2.2 that there are three composition ranges of Mg which lead to varying graphite shapes and there is a minimum of 0.03% to obtain nodular graphite particles [19]. Nodularity is defined as the ratio of the area fraction exceeding a critical curvature (for which the graphite particles are considered as nodular shaped) to the total area fraction of graphite [20]. Other spheroidizers include calcium and Rare Earth Metals (REM) such as lanthanum and cerium are also used as spheroidizers. While calcium is used to reduce the volatility of magnesium reaction and improve magnesium recovery, REMs in optimum combinations with magnesium increase the number of nodules [15].

## 2.6. Microstructure of High Silicon – Molybdenum Cast Iron

The microstructure of SiMo ductile cast irons consists of nodular graphite particles embedded in ferritic matrix with small amounts of grain boundary carbides. Black et al. [21] found an anomalous microstructure constituent which was initially assumed to be

pearlite. However, this constituent was often found in the as-cast state only at the grain boundary regions as a fine precipitate with non-lamellar character.

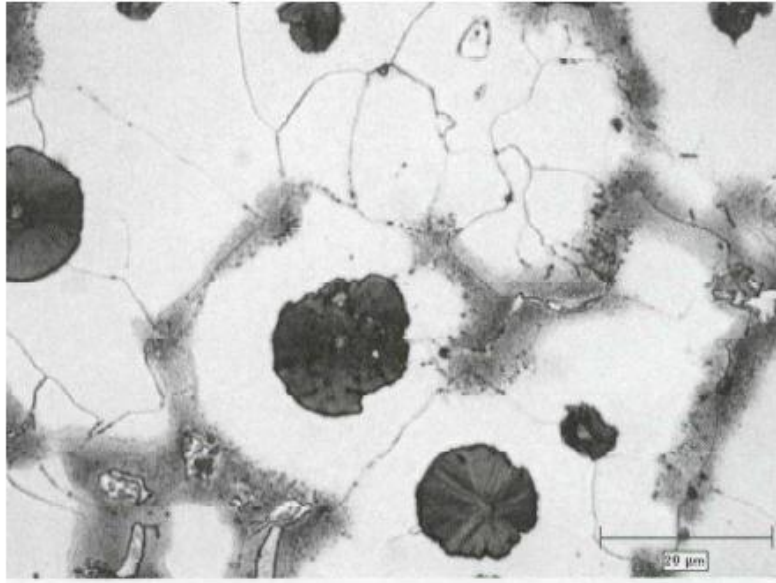


Figure 2.3 Typical microstructure of SiMo ductile cast iron [21]

It was demonstrated [17] that the fine precipitates are often mistakenly identified as pearlite structures. The fine precipitates found in the grain boundary regions are eutectic carbides and are pearlite free because of the high Si content and the inoculation process during casting. However, some amount of pearlite can be formed in the case of unusual processing conditions such as fast cooling rates or due to the presence of moderate levels of Mn and tramp elements [21].

### **Carbide phase**

The fine precipitate phase is found to be a Mo-rich phase. This was supported by the fact that the precipitate phase were absent in Mo- free high Si ductile cast irons. The precipitates were confined to the grain boundaries as eutectic carbides due to molybdenum segregating strongly during solidification. Analysis of selected area diffraction patterns obtained from these precipitates has identified two structures, with lattice parameters equivalent to those for  $\text{Fe}_2\text{MoC}$  and  $\text{M}_6\text{C}$  [21] [17].

The  $\text{Fe}_2\text{MoC}$  and  $\text{M}_6\text{C}$  precipitates are believed to precipitate under slow cooling rate conditions in the ferrite matrix after the proeutectoid and eutectoid transformations are complete. Under faster cooling rates only ferrite and pearlite are formed. There are no grain boundaries between the precipitate and ferrite regions – a feature observed with eutectoid transformation [21]. The precipitation of  $\text{Fe}_2\text{MoC}$  and  $\text{M}_6\text{C}$  phases occur only

in regions where Mo concentration is high – the cell boundary regions where the local concentration of Mo is increased due to segregation on solidification. The value of Mo concentration is found to be about 1% below which the phases are not thermodynamically stable [14] [21].

### Dimensional Stability

The temperature at which the phase transformation starts to occur from ferrite to austenite is called the Ac1 temperature. This phase transformation occurs along with a loss of dimensional stability. Thus exhaust manifolds made of standard SiMo materials are used in operation conditions much below their Ac1 temperatures (830 °C) [5] [6]. The Fe<sub>2</sub>MoC type carbide is found to be stable and will not decompose to ferrite and graphite at operating temperatures. The precipitates are found to be stable up-to 1000 °C after which they dissolve. The precipitate phase, which is a unique characteristic of SiMo ductile irons, is an advantage over pearlite containing high Si ductile cast irons. The presence of this precipitate phase provides dimensional stability at temperatures below Ac1 unlike pearlite [21]. Additionally, Si and Mo increase the Ac1 temperature as seen in figure 2.4 and thereby increase the operational temperature range of the material.

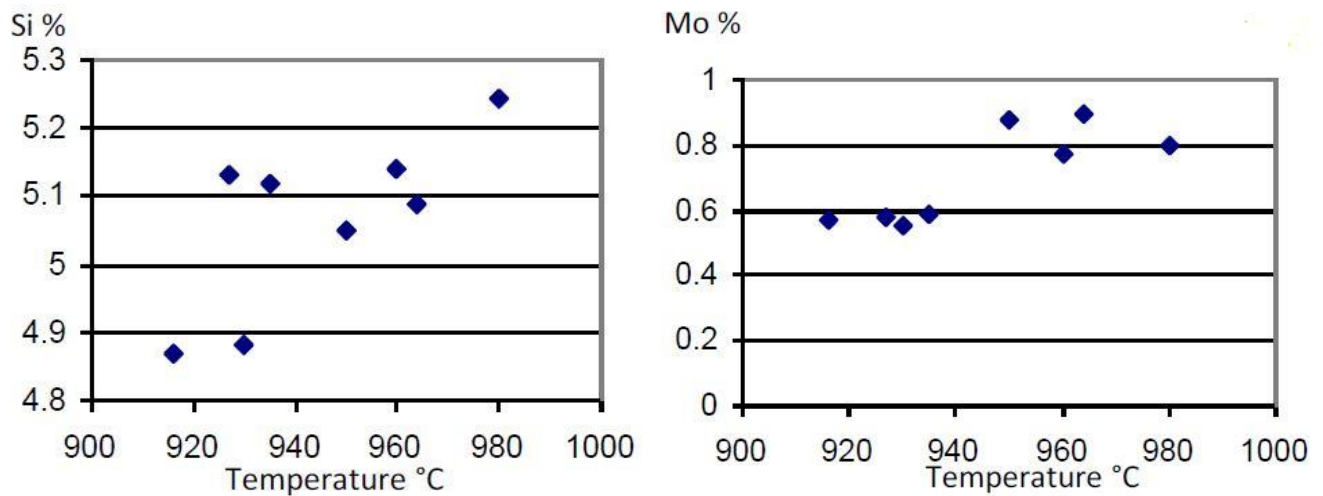


Figure 2.4 Influences of Si and Mo on Ac1 temperature [6]

## 2.7. Heat-treatment of Silicon-Molybdenum Ferritic Cast Iron

Not much literature has been published studying the effect of heat-treatment on SiMo cast iron. Generally, a heat treatment for ferritic SiMo ductile iron is performed for dissolving intercellular carbides to improve ductility and dimensional stability [17]. A comparison of microstructural characteristics and other material properties of heat-treated and as-cast conditions to study the influence of heat-treatment in SiMo cast iron

were done by Li et al [17]. The heat treatment carried out was similar to the current heat-treatment process that DAF trucks' exhaust manifolds undergo – refer table 2.1

Figure 2.6 (a) shows the as-cast microstructure of SiMo cast iron. It is seen that heat treatment disperses the fine Mo-rich precipitates that are present in as-cast conditions, away from the grain boundary regions. Sub-critical and full anneal seemed to promote precipitate distribution within the ferritic matrix as seen in figure 2.6 (b). However, no useful modification to the Mo-rich phases is seen. Though heat-treatment brought about some microstructural homogenization, no appreciable change was noted in the graphite phase or grain size [17].

**Table 2.1 Heat-treatment steps followed by Li et. al and current process for exhaust manifolds at DAF trucks**

Heat-treatment steps	Li et. al.	DAF trucks
Step1: Sub-critical annealing	At 785 °C for 3 hours	At 740 °C for 3 hours
Step 2: Full annealing	At 940 °C for 3 hours	At 900 °C for 3 hours
Step 3: Slow cooling	To 650 °C at 100 °C/h	To 640 °C at 100 °C/h
Step 4	Air cooling	Air cooling

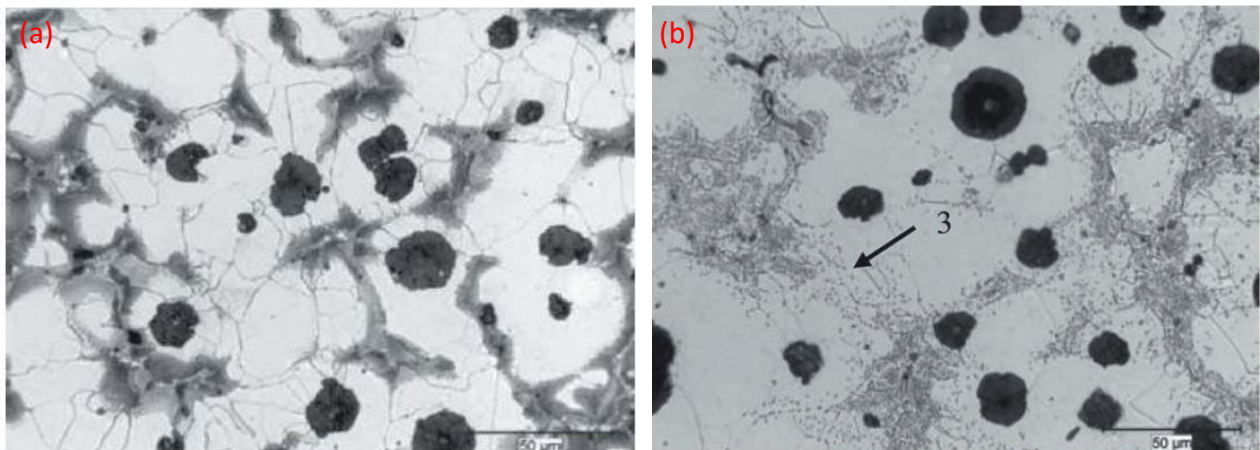


**Figure 2.5 Ferritic SiMo ductile iron a) as-cast state b) fully annealed state [16]**

## 2.8. Mechanical Properties of Silicon – Molybdenum Cast Iron

At intermediate alloying (4-6%), Si is effective in and increasing the hardness of the ferritic matrix. By solid solution strengthening of the ferrite matrix, silicon contributes to the mechanical properties of SiMo ductile cast irons. Numerous literatures are available on the effect of Si and Mo on the mechanical behavior of ductile cast irons at room and elevated temperatures [13] [22] [23] [24].

There exists a critical value of Si content (~3.5%) below which the tensile strength and elongation increases with increasing Si content and above which the mechanical properties decreases sharply [25]. Irons with silicon contents above 5% are more likely to be brittle and hence the silicon content is limited to below 5% for service [9]. This was confirmed [13] by studying Si content above the critical value and the Mo content between 0.5-0.9%. The ultimate tensile strength (UTS), yield strength (Y) and Brinell hardness (HBW) increase, while the elongation and impact toughness decrease with increasing Si content as seen in figure 2.6. However, it was observed that silicon does not significantly affect the Young's modulus [24].

Martinez et al. [24] investigated the effect of Si content between 3.8–6.1 % on the mechanical behavior by studying room temperature tensile stress-strain curves. The Increasing the silicon content increases the UTS value up to 5.2 % above which the UTS decreases. The decrease goes along with a marked reduction of the tensile elongation up to a point where there is no plastic deformation for the highest silicon content [24].

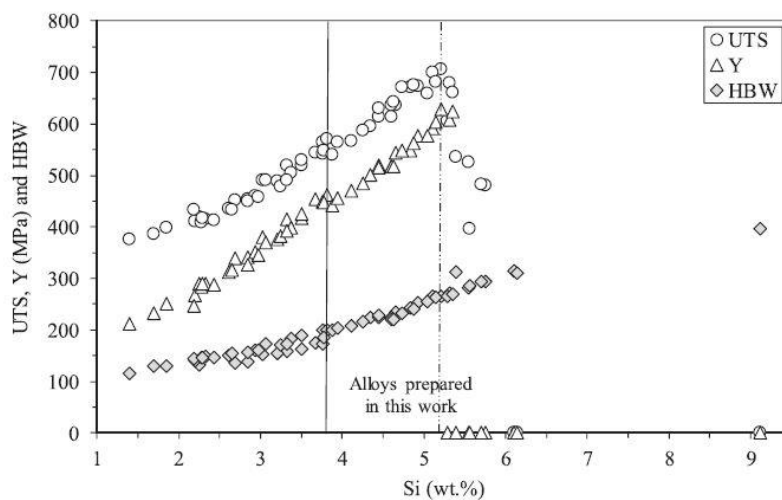


Figure 2.6 Evolution of UTS, Y and HBW with Si content at room temperature [24]

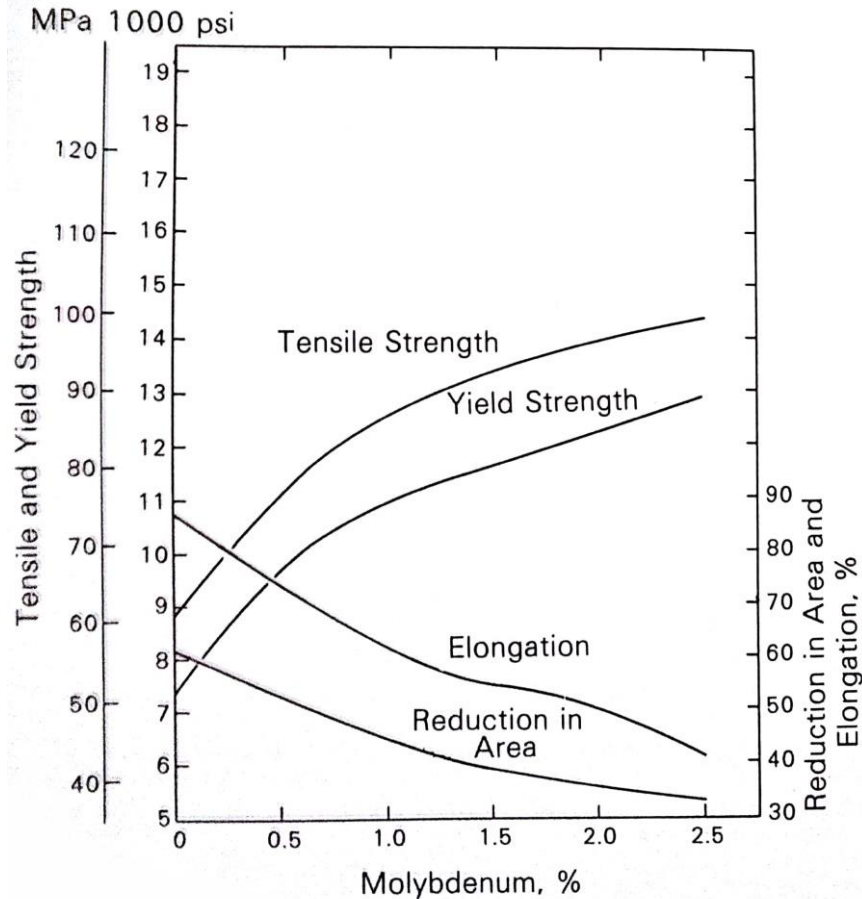


Figure 2.7 Effect of Molybdenum on Tensile properties at 705 °C at 4% Si [9]

The solid solution strengthening effect of Si seems to diminish at temperatures above 500°C. At temperatures of 700 °C and 900 °C the UTS decreases with increasing Si as the carbon solubility is reduced by Si, causing carbon to dissociate as carbides [13]. For this reason primarily, molybdenum is added to provide high temperature mechanical properties for intermediate silicon ductile irons. The 4% silicon ductile cast irons are alloyed with 0.6 to 2% molybdenum to combine adequate strength and ductility at room temperature with high strength and oxidation resistance at high temperatures. The improvements in yield and tensile strengths of 4% silicon ductile cast iron at 705 °C on alloying up to 2.5% molybdenum content [9] can be seen in figure 2.7. Figure 2.8 shows the creep rupture properties of 4% Si ductile iron alloyed with 1-2% Mo. Although there is an increase in creep rupture strength and creep properties as molybdenum content is increased from 0 to 2.5%, the greatest response to Mo content is seen at 0.5 to 1% alloying.

Ferritic SiMo ductile cast irons exhibit low elongation of less than 3% at temperatures around 425 °C. This reduction of ductility at medium temperatures is referred to as mid temperature brittleness. This is a known, detrimental effect for high temperature applications of ferritic ductile cast irons. Lui et al [23] investigated the high temperature mechanical properties of ferritic ductile cast iron and observed a brittle behavior at 400 °C. This effect has also been reported and observed in many literatures [9] [13] [17].

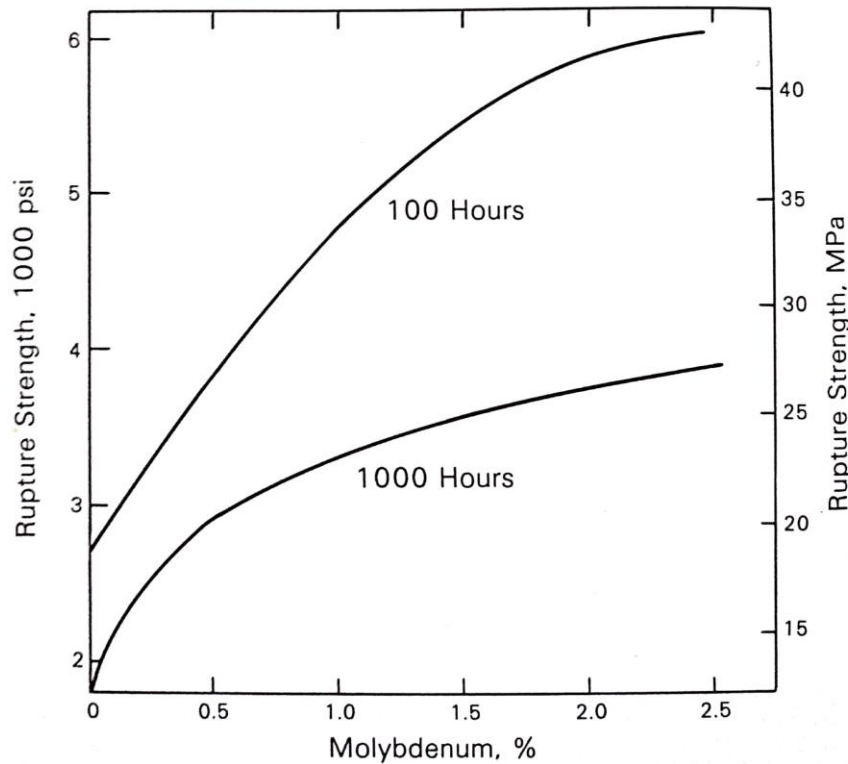


Figure 2.8 Creep rupture properties of 4% Silicon ductile cast iron with increasing Mo content [9]

Li et al. [13] studied the effect of heat-treatment on the ductility of SiMo ductile cast irons. HiSiMo sample bars were made to undergo the heat treatment procedure as mentioned earlier. The heat-treatment seemed to improve the ductility of high silicon SiMo cast irons, marked by an increase in elongation. The increase in ductility is attributed to the reduction of the Mo-rich phases. The amount Mo-rich phases were found to reduce on heat-treatment from 7.3% (as-cast), to 6.4% (subcritical annealing), and to 3.2% (full annealing).

Charpy tests were conducted [17] on un-notched rectangular specimens (10 x 10 x 55mm). It is found that there is no significant change in room temperature Charpy toughness values of SiMo ductile cast irons after heat-treatment. The Charpy toughness

values were observed to exhibit a stronger dependence on Si and Mo content rather than on heat-treatment. The average impact toughness value decreased from 35J to 10J when the Si content was increased from 4% to 5%. A similar trend was also observed with increasing Mo content in SiMo ductile cast irons.

The ultimate tensile strength and yield strength dropped slightly on heat-treatment [13] [17]. It was concluded that there is no significant change in tensile properties, hardness and Charpy toughness at room temperature by the annealing treatment mainly because the SiMo microstructure is already ferritic and pearlite free in as-cast conditions. No effect on mid temperature brittleness by heat-treatment was observed [17]. Although annealing promotes a slight increase in tensile elongation at room temperature, no such effect was observed at 425°C. However, phosphorous alloyed SiMo samples showed high elongations at 425 °C and similar elongations as non-alloyed phosphorous alloys at low temperatures. Mid temperature brittleness is reported to be caused by magnesium and sulfur assisted grain boundary segregation of impurities. Controlling the amounts of sulfur and magnesium and adding small amount of phosphorous increased the elongation at medium temperature from 2% to 19% for SiMo ductile cast irons [17]. Table 2.2 presents the yield strength ( $R_p$  0.2%), ultimate tensile strength ( $R_m$ ) and elongation at fracture ( $A_5$ ) at different temperatures for non-heat-treated and heat-treated SiMo 5.10 cast iron obtained from monotonic isothermal tensile tests.

**Table 2.2 Comparison of Tensile properties of a) Non-heat-treated and b) heat-treated SiMo cast iron at different temperatures**

(a)				(b)			
Temp (°C)	$R_p$ 0.2% (MPa)	$R_m$ (MPa)	$A_5$ (%)	Temp (°C)	$R_p$ 0.2% (MPa)	$R_m$ (MPa)	$A_5$ (%)
20	444	544	6.7	20	494	590	10.5
200	394	525	7.0	200	N/A	N/A	N/A
300	435	560	7.6	300	431	551	7.6
400	408	536	6.7	400	401	529	7.1
450	395	500	7.5	450	388	488	8.6
500	376	418	10.9	500	370	407	11.7
600	219	229	19.9	600	208	215	20.7

## 2.9. Thermo-mechanical Fatigue (TMF) Concepts

To better understand the literature on *TMF*, the testing performed in the current work and the discussion that follows, it is important to shed light on some of the important concepts involved. The basics of *TMF*, parameters in testing and also *TMF* lifetime prediction techniques are briefly explained below.

## 2.10. Thermal and Mechanical Strains in *TMF*

An exhaust manifold subject to thermo-mechanical loading develops thermal and mechanical strains given by:

$$\epsilon_{net} = \epsilon_{th} + \epsilon_{mech}, \quad (2.2)$$

where  $\epsilon_{net}$  is the net or total strain developed during a single thermo-mechanical fatigue cycle as the sum of thermal strain,  $\epsilon_{th}$  and mechanical strain,  $\epsilon_{mech}$ . The thermal strain is given as

$$\Delta\epsilon_{th} = \alpha\Delta T, \quad (2.3)$$

where  $\alpha$  is the co-efficient of thermal expansion of the material and  $\Delta T$  is the temperature range of the *TMF* cycle. The mechanical strains develop due to the externally applied constraints to thermal expansion. The amount of constraint for a given system can vary between more than 100% in the case of over-constraint to 0% in the case of no-constraint or total free expansion. However, in an engine component total constraint condition (100%) is the most severe condition possible. The amount of constraint is denoted by  $\gamma$ , which relates the thermal and mechanical strains developed in the component during thermo-mechanical loading, is described by:

$$\epsilon_{mech} = -\gamma \cdot \epsilon_{th}, \quad (2.4)$$

where,

$\gamma > 1$  for over constraint,

$\gamma = 1$  for total constraint,

$0 < \gamma < 1$  for partial constraint and

$\gamma = 0$  for no constraint

## 2.11. Out-of-phase *TMF*

Engine components including exhaust manifolds undergo out-of-phase (OP) thermo-mechanical loading during operation i.e. compressive strains develop during the heating cycle whereas tensile strains develop during the cooling cycle. There is a 180 degree

phase shift between the temperature cycle and the mechanical strain developed as shown in figure 1.1.

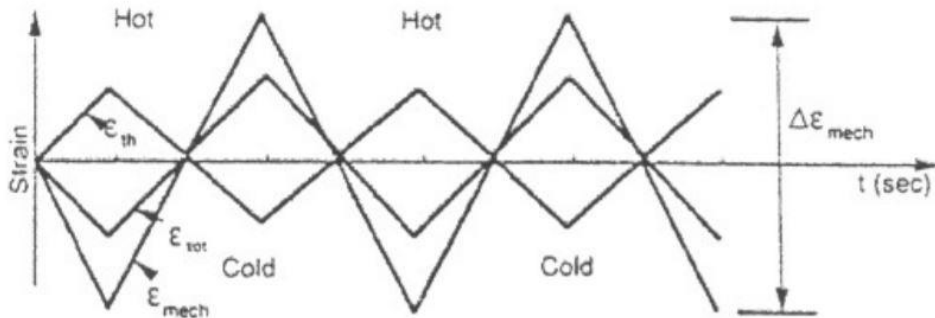


Figure 2.9 Temperature-Strain variations with respect to time in OP TMF [26]

### 2.12. Holding time in TMF

The amount of time the component is at the maximum temperature ( $T_{max}$ ) or at the minimum temperature ( $T_{min}$ ) during a single TMF cycle is called holding time ( $t_{hold}$ ) in TMF. Holding time at high temperature is an important parameter in TMF testing as it promotes stress relaxation – a well-known dominant damage mechanism in TMF. The stress relaxation as a result of a holding time at high temperature is illustrated in figure 2.10.

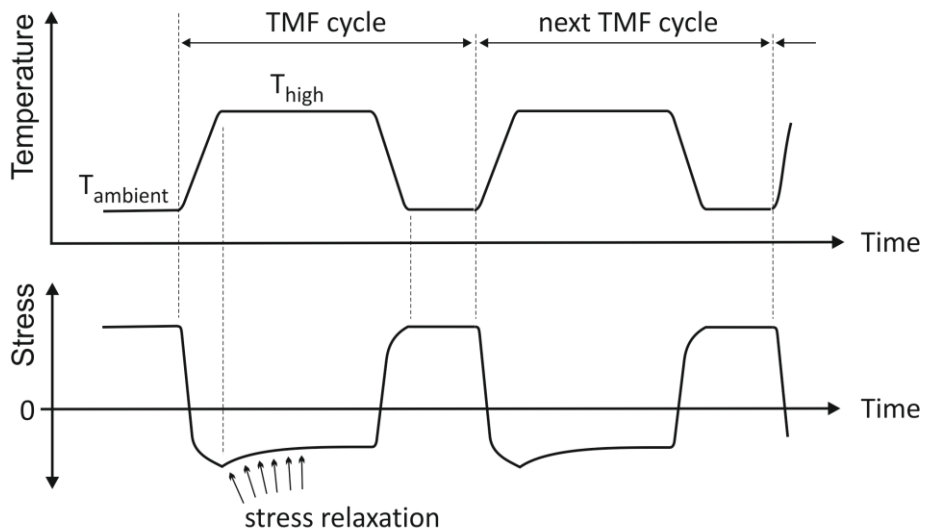


Figure 2.10 Schematic illustration of stress relaxation during holding time at high temperatures [20]

### 2.13. Prediction of TMF lifetime

Numerical estimation of thermo-mechanical fatigue lifetime has been done previously using Paris equation 2.5 for fatigue crack growth. Ghodrat [20] was able to accurately predict the TMF lifetime of compacted graphite cast iron using the Paris model despite the extensive plasticity that develops. Zafeiropoulos [27] was also able to implement the Paris crack growth model for SiMo nodular cast iron to find TMF lifetimes.

$$\frac{da}{dN} = C(\Delta K_I)^m \quad (2.5)$$

In the above mentioned works, the numerical estimates were performed only for total constraint conditions. Since total constraint conditions are considered harsher than real life service conditions, Kalra [4] applied the Paris law for other constraint levels as well. It was found that a universal Paris expression 2.5 could be obtained as a function of mechanical strain range applicable to all constraint conditions considered. The units of  $\Delta K$  and  $\frac{da}{dN}$  in equation 2.6 are  $MPa m^{0.5}$  and  $m$  respectively.

$$\frac{da}{dN} = \{(\Delta \varepsilon_{mech} \times 10^{-7}) - 3 \times 10^{-10}\}(\Delta K)^{3.60} \quad (2.6)$$

### 2.14. Thermo-mechanical Fatigue in Silicon – Molybdenum Cast Irons

The effect of alloying elements and the mechanical properties of SiMo cast irons at various temperatures have been characterized thus far. Numerous studies have also been carried out on Low Cycle Fatigue (LCF) [12] [28] [29], thermal fatigue [3] [30] and thermo-mechanical fatigue (TMF) [2] [11] [31]. Since high temperature fatigue is one of the major causes of reduction in the longevity of exhaust manifold components [2], it is important to understand the thermomechanical loading conditions and the material behavior under such conditions.

It is with this intention the thermal fatigue behavior of SiMo 5.10 material (C – 3.1%, Si – 4.7%, Mo – 1.1%) has been studied in [3]. Thermal fatigue samples were tested at different maximum temperatures between 700 °C and 900 °C with a holding time of 10 minutes and quenched with running water at 20 °C. Repeated thermal cycles caused surface cracks in the specimens and it was found that  $da/dN$  increased with increasing  $\Delta T$ . The source of crack initiation due to thermal cycling was found in the Mo-rich eutectic cell boundary regions. The repeated thermal cycling caused oxidation of the Mo-rich eutectic phases which promoted grain boundary embrittlement. The eutectic oxides in the grain boundaries allows for the formation of a high strain zone around which many thermal cracks were seen. During the cooling cycle, due to the thermal gradient between the hotter core and cooler surface of the specimen, tensile stresses

are produced on the surface and compressive stresses are produced in the core. This repeated thermal cycling causes internal thermal stresses which result in plastic strains in the specimen. These leads to thermal fatigue crack [3] [8] [32].

It should be explained here that the difference between thermal fatigue and thermo-mechanical fatigue is arbitrary [32]. In the case of thermal fatigue, the thermal cycling without external loads causes internal stresses due temperature gradients and/or thermal expansion mismatch as seen above. However, in the case of thermo-mechanical fatigue, similar stresses and strains are caused by simultaneous application of thermal and externally applied mechanical loads [8] [20].

The comparison of the isothermal LCF behavior between SiMo 5.10 (C - 3.07% Si - 4.58% Mo - 1.1%) and SiMo 4.05 (C - 3.43% Si - 3.83% Mo - 0.40%) materials for exhaust manifold application [29] showed the effect of composition on high temperature fatigue performance of the materials. Both the materials were tested isothermally at 600 °C and 800 °C at a constant strain rate of 0.001/s. It was found that an increase of Si and Mo contents increases the fatigue life of SiMo cast irons.

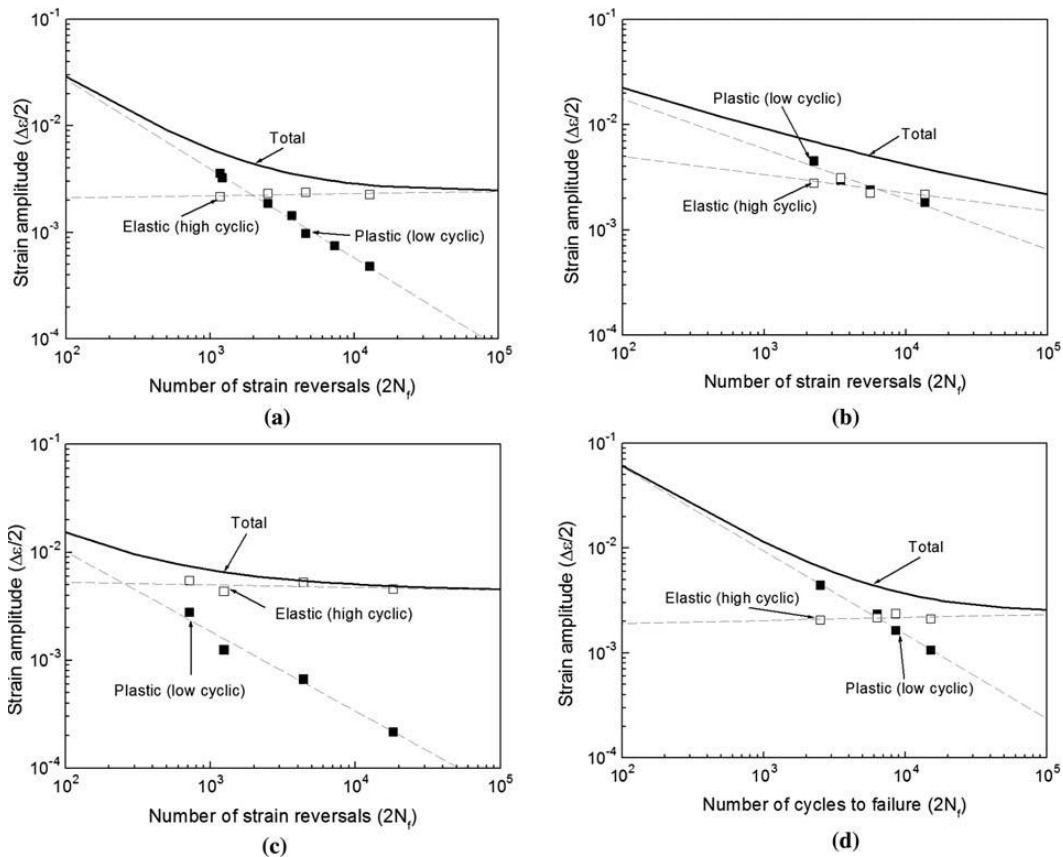


Figure 2.4 Fatigue strain-life curves plotted by the superposition of elastic and plastic cyclic strain conditions: (a) SiMo 4.05 at 600 °C, (b) SiMo 4.05 at 800 °C, (c) SiMo 5.10 at 600 °C, and (d) SiMo 5.10 at 800 °C [29].

At 800 °C, SiMo 5.10 performs better than SiMo 4.05 for all strain ranges. However at 600 °C, both the alloys show similar fatigue life at strain ranges between 0.5% and 0.6%; but at other strain ranges SiMo 5.10 showed lower fatigue life.

A Coffin-Manson type equation was introduced to address this. It can be seen from figure 2.10 that at 600 °C, the transition from low cycle fatigue to high cycle fatigue conditions occurs at  $2N_f = 1920$  and  $\Delta\varepsilon = 0.45\%$  for SiMo 5.10, while for SiMo 4.05 at  $2N_f = 256$  and  $\Delta\varepsilon = 1.02\%$ . The difference in fatigue behavior was explained by the fact that SiMo 5.10 is relatively stronger and less ductile at 600 °C. Thus, for the same input total strain amplitude, the stress concentration around the graphite nodules increases causing fatigue failure to occur after a shorter time. This effect was not seen at higher temperature of 800 °C because then the fatigue behavior becomes more complicated due to severe oxidation.

Since it was concluded that the major damaging mechanism of LCF at high temperature is oxidation [29], similar LCF tests were performed on SiMo 5.10 by Wu. et al. [28] to develop a holistic damage model given by equation 2.6 which considers multiple forms of damage developing in the material during thermo-mechanical loading:

$$\frac{da}{dN} = \left(1 + \frac{1}{\lambda}\right) \left\{ \left(\frac{da}{dN}\right)_f + \left(\frac{da}{dN}\right)_{ox} \right\} \quad (2.7)$$

Where  $\left(\frac{da}{dN}\right)_f$  is the fatigue contribution, and  $\left(\frac{da}{dN}\right)_{ox}$  is the oxidation contribution and  $\lambda$  is the crack/cavity inter-spacing in  $\mu\text{m}$  [28].

Experiments were performed at strain rates of 0.02/s, 0.002/s and 0.0002/s in different temperature ranges between room temperature and 800 °C. It was determined that the cyclic stress-strain response of the SiMo cast irons is the result of plasticity-creep interaction for a given strain rate and temperature. It can be seen that with increasing temperature and decreasing strain rate, the stress is reduced with the onset of time dependent (creep) deformation. At high temperatures, the formation of oxide films did not change the stress but affects material life [28] [29].

As seen earlier in this section, many damage models have been developed to study TMF behavior through isothermal LCF test data. This methodology is often futile as it does not recognize all the damage that occurs during temperature dependent strain conditions during TMF [20]. Since TMF loading can be more damaging than isothermal LCF conditions, it is important to distinguish between the two. Wu et. al. [11] performed thermo-mechanical fatigue testing in SiMo cast irons and also predicted lifetimes with the Integrated Creep Fatigue Theory (ICFT) model. ICFT was used in finite element

method with the consideration of four deformation/damage mechanisms: plasticity-induced fatigue, intergranular embrittlement, creep, and oxidation.

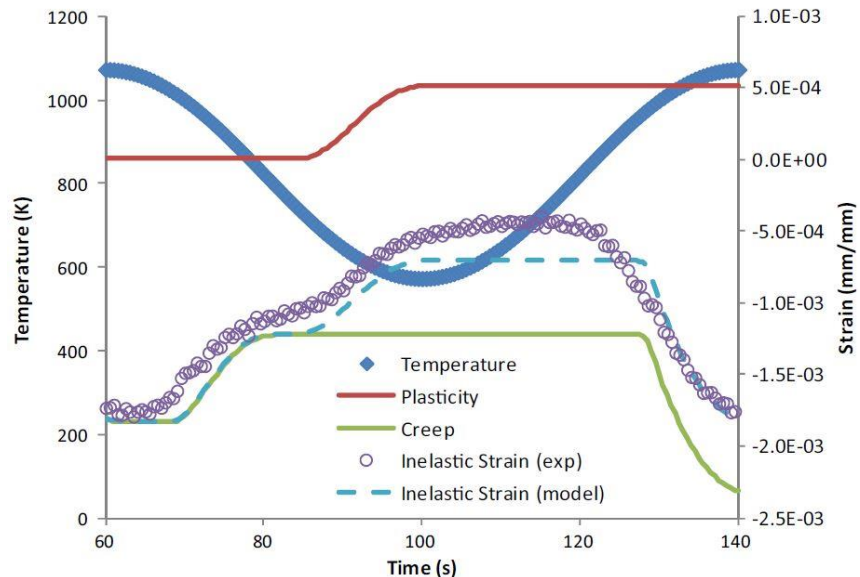


Figure 2.5 Strain accumulation during OP-TMF in the range of 300 °C to 800 °C [11]

TMF testing was performed on two SiMo cast irons. The first material was alloyed with 4.10% Si and 0.60% Mo. The second material contained 4.30% Si and 0.97% Mo. Both OP and IP tests were conducted in the temperature range 300 °C ( $T_{min}$ ) to 800 °C ( $T_{max}$ ) for different constraint ratios,  $\gamma = 1, 0.7$  and  $0.6$ . The development of inelastic strain during an OP TMF cycle is shown in the figure 2.12. The inelastic strain, which is the resultant of the creep strain and the plastic strain, exhibits a stabilized behavior in the mid-life TMF cycle. The ICFT model used to predict the variation of inelastic strains during OP-TMF showed good agreement with the measured value. The creep deformation dominated during the hot part of the cycle, and plastic strain arose during the cold part of the cycle, reversing the compressive creep deformation [11].

# 3. Experimental Approach

## 3.1. TMF Test Specimen and Material

Three types of SiMo cast iron alloys were tested in this study. The materials were cast using serial casting process to produce Y-shaped blocks. Each block gives one test bar which is machined to the final geometry as shown in figure 3.1 and supplied by Georg Fischer foundry in batches. Each batch consisted of 10 specimens. The specimens were circumferentially notched at TU Delft by a turning operation before testing. The notches were machined within a tolerance of 0.01 mm. Additional care was taken to radially align the specimen before notching operation by using a four radial jaw chuck and manually adjusting the jaws while simultaneously checking for optimal eccentricity using a micrometer probe. Refer to [4] and [20] for more information on the notching procedure.

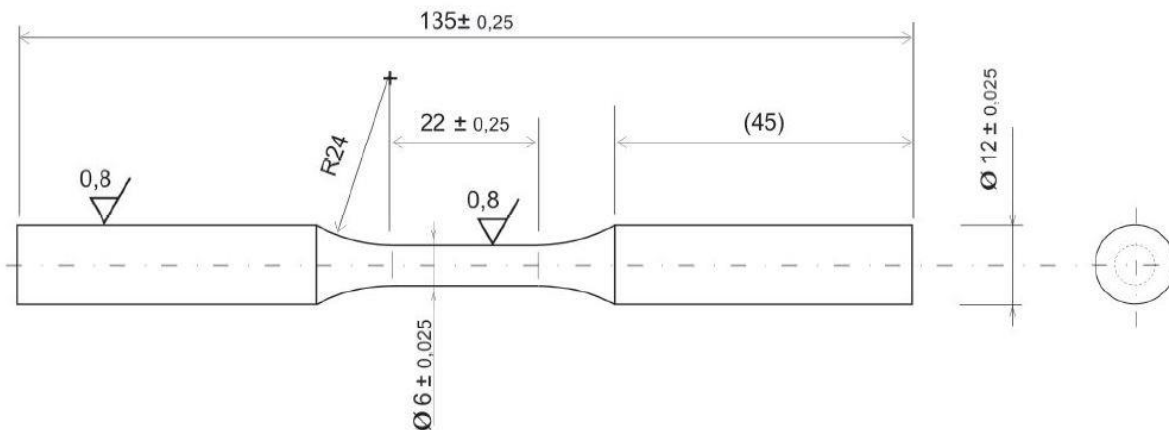


Figure 3.1 Dog-bone specimens designed for TMF tests

All the materials investigated in this study consist of a predominantly ferritic matrix with uniformly distributed graphite nodules and Mo-rich eutectic phases. According to DAF standard for casting alloyed nodular cast iron, the structure is allowed a maximum of 20% pearlite and a maximum of 4 % carbides. The graphite must be at least 90% segregated in the form of type V and VI nodules in accordance with ISO 945-1 [33].

Table 3.1 summarizes the materials investigated in this study and their respective compositions. The materials are assigned a code for ease of discussion. Codes A1 through A3 represent the different batches of SiMo 5.10 material. It should be mentioned here that the batch D of SiMo 5.10 material initially supplied by Georg Fischer foundry was mistaken to be non-heat treated specimens. Thus, both batches D

and X consisted of heat-treated SiMo 5.10 specimens. The batch N which consists of non-heat-treated SiMo 5.10 specimens were supplied and tested much later. SiMo 4.05 and SiMoNi materials are represented by B1 and C1 respectively.

**Table 3.1 Chemical Composition of SiMo cast irons tested**

Material			Chemical composition [weight %]						
Designation	Batch	Code	C	Si	Mo	Mn	P max.	Ni	Fe
SiMo 5.10	D	A1	3.25	4.45	0.76	0.26	0.02	-	remainder
	X	A2							
	N	A3							
SiMo 4.10 <sup>b</sup>	-	A4	3.4	4.2	0.8	0.5	0.05	0.02	remainder
SiMo 4.05	-	B1	3.22	4.66	0.56	0.25	0.02	-	remainder
SiMoNi	-	C1	3.3	4.5	≤ 1	≤ 0.4	-	1- 1.3	remainder

Since this is a comparative study of *TMF* performance of different materials, only single notch depth was used. Notch with depth 0.15 mm was employed on all the specimens tested. The advantages of testing with notched specimens are two-fold. Firstly, they reduced the testing time due to longer initial crack length and secondly, they also reduced the scatter in life-time results. Ghodrat [20] found that for small notches between 0.1 to 0.2 mm, there is no significant decrease in stiffness due to the presence of the notch. Although, the maximum stress developed is limited by the smaller amount of *TMF* cycles to failure, the stress levels developed during the initial *TMF* cycles are similar to that of smooth specimens.

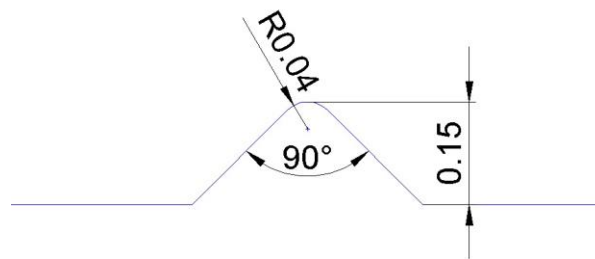


**Figure 3.2 Notch specifications that is employed in all specimens for TMF testing [4]**

<sup>b</sup> Tested by Kalra [4]

### 3.2. Experimental Set-up

The *TMF* set-up employed consists of a number of components built around a fatigue testing machine which work in unison to perform a successful *TMF* test. The complete *TMF* set-up used is shown in figure 3.3 (a) and explained in detail below.

The test set-up mainly consists of an MTS 858 table top machine which is a servo-hydraulic fatigue testing machine. The capacity of the machine is 25 kN in both compression and tensile directions. The dog-bone specimens to be tested are held in the fatigue testing machine in the hydraulic upper and lower grips using smooth collets. Care is taken to align the two grips axially and concentrically settings to prevent any buckling during testing. It should be noted that both grips are water cooled; and the cooling is optimized by maintaining the temperature of both the grips at (equal) room temperature to prevent development of thermal gradients in the gauge section of the specimen.

A Hunttinger Ultra High Frequency (UHF) induction generator is used to heat the specimens with an induction coil. The specimen is placed in the grips such that the coil is positioned around its gauge length. The samples are heated by induction heating – a non-contact heating principle which heats only the outer surface of the specimen by producing eddy currents. The inner part is heated by conduction from hot surface to the cold inner core. A heating rate and cooling rate of  $7.1^{\circ}\text{Cs}^{-1}$  and  $5.5^{\circ}\text{Cs}^{-1}$  respectively is used in accordance to the temperature profile calculations [27]. The temperature of the specimens is measured using three K-type thermocouples. The ends of the thermocouple wire were welded to form a loop which is securely wrapped around the gauge length of the specimen and made sure that they are in contact. The three thermocouples are placed equidistant from each other (5mm) within the gauge section of the specimen used by the extensometer (see below). The center thermocouple, which is used to control the temperature, is placed 1 mm above the notch.

During the cooling cycle, the temperature of the specimen is reduced by gradually reducing the heat input and then by blowing air on the gauge section using three nozzles. The nozzles are directed at the gauge section of the specimen from different directions to ensure uniform cooling. The axial strain or net strain was measured using a strain gauge extensometer which uses of ceramic contact rods forming a gauge length of 12 mm and has a maximum operating temperature of  $1200^{\circ}\text{C}$ . The extensometer apparatus is shielded from the high temperature of the specimen by providing adequate cooling by blowing compressed air. The air-cooled ceramic rod extensometer and other components discussed above can be seen in figure 3.3 (b).

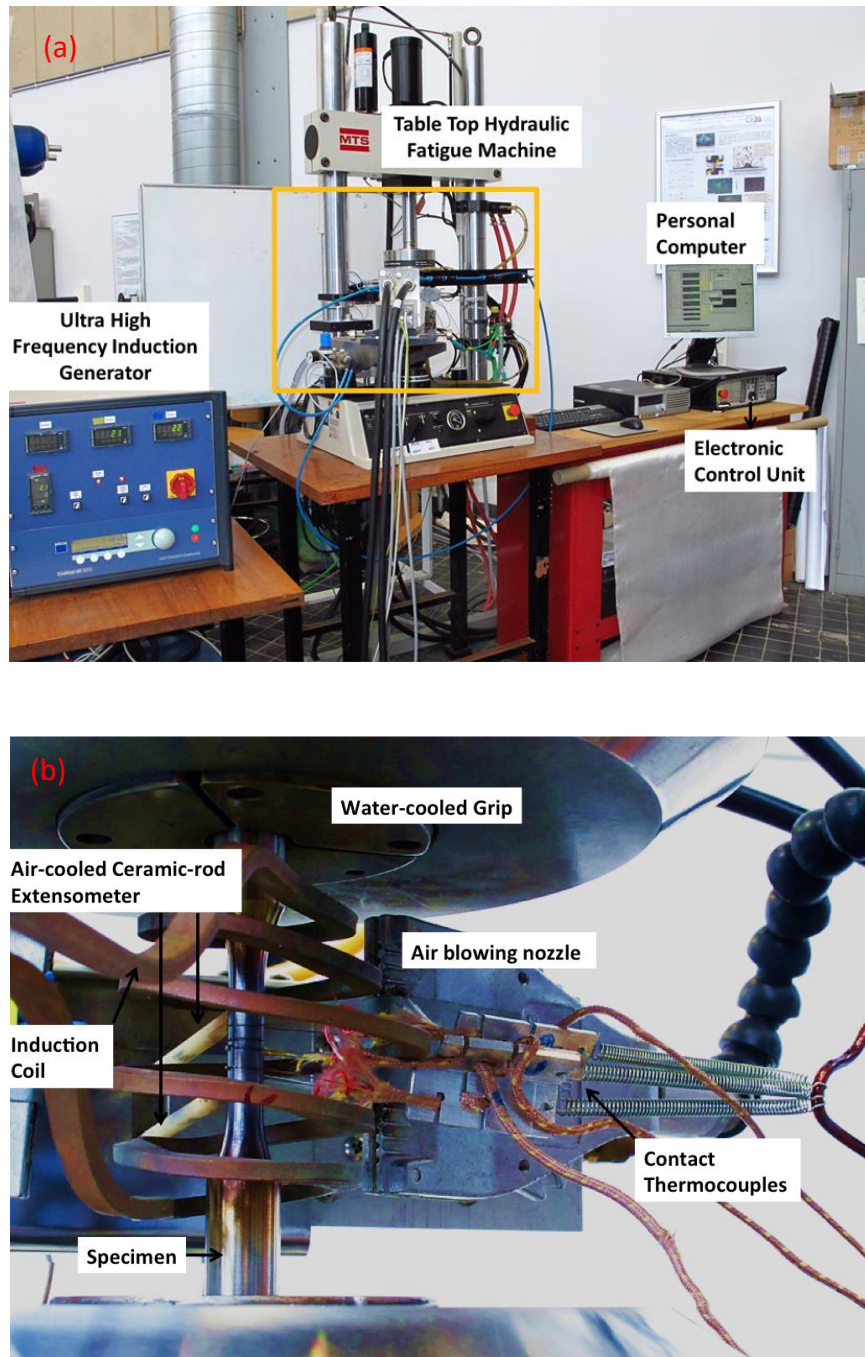


Figure 3.3 TMF Machine set-up (a) The entire set-up (b) Close-up view [20]

A TMF test is designed and controlled by a personal computer using dedicated Model 793.00 system software in combination with Multiple Purpose Testware (MPT). The physical command controls to the TMF set-up are fed through an electronic unit Flextest™ SE version, in a control loop. The machine can be operated using channels

which can generate command signals. The inputs to these channels are called set-point values.

The three main channels are the axial channel, the temperature channel and the cooling channel. The axial channel consists of three control modes – strain control, CLC or displacement control and force control. It should be noted here that since the three control modes are interdependent, the set-up can be controlled using only one of them at a given time. The channels along with the control modes are operated using the MPT software. It uses a graphical test programming interface which enables the user to select data acquisition processes, trigger processes and create a test procedure which consists of a set of sequential actions to be executed by the fatigue testing machine. The *TMF* tests are designed to investigate the failure mechanism of the materials by acquiring the required data and determining the number of cycles to failure.

### 3.3. TMF Test series Performed

The included materials (see table 3.1) in this study are tested under partial constraint condition of 75% since total constraint condition was deemed harsher than real life service conditions [4] [27]. A *TMF* test procedure is designed by cycling the temperature between  $T_{min}$  and  $T_{max}$  with a holding time of  $t_{hold}$ . The general procedure of a *TMF* test with partial constraint condition and the corresponding stress-strain hysteresis loop that develops during the *TMF* cycle is explained as seen in figure 3.4 and 3.5 in terms of sequential steps.

**Test initiation:** First, the specimen is placed in the grips and clamped. As clamping seemed to increase the load on the specimen, care is taken to reduce to load value to zero before the test initiation. During the test initiation phase, the load level is constantly maintained at zero until the specimen is heated to  $T_{min}$ . Then, the control mode is switched from load control to strain control and the partial constraint condition ( $\gamma = 0.75$ ) is applied.

**Partial Constraint:** Unlike total constraint condition, some free expansion and contraction occurs during partial constraint. This is implemented in the test program by independently controlling the strain channel along with the temperature channel. The programmed extensometer strain set-points are obtained from equations 2.2, 2.3 and 2.4:

$$\epsilon_{net} = (1 - \gamma)\alpha\{T_{max} - T_{min}\}, \quad (3.1)$$

where  $\alpha$  is the coefficient of thermal expansion.

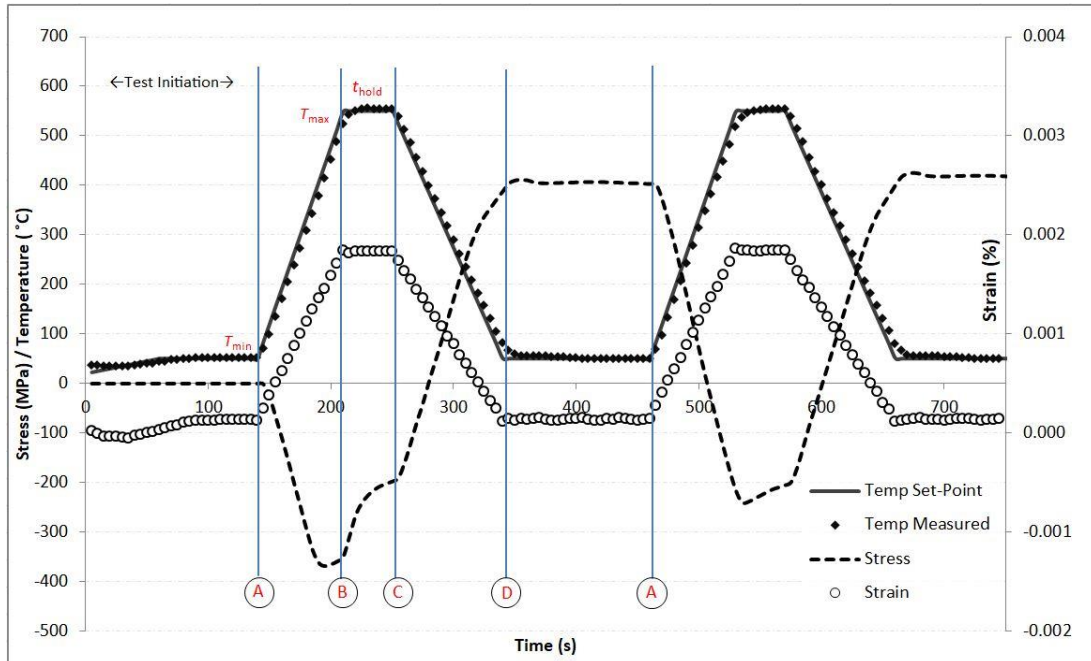


Figure 3.4 Typical signal response as a function of time for a TMF test under partial constraint

**Sequence A→B:** The specimen is heated gradually from  $T_{min}$  to  $T_{max}$  at a constant heating rate as mentioned earlier. Simultaneously, the strain is increased to a set point calculated according to equation 3.1. It should be noted that the strain value set in the program (and measured by the extensometer) is the net strain value (sum of thermal and mechanical strain). The stress is calculated from the load signals measured by the load cell. It can be seen in figure 3.5 that the material experiences increasing compressive stresses and starts yielding during this sequence. The material hardens on further heating and it should be noted that the maximum compressive stress is not achieved at  $T_{max}$  as the material experiences some softening at  $T_{max}$  (Point B).

**Sequence B→C:** The temperature at  $T_{max}$  and also the corresponding extensometer strain set-point are held constant for a programmed holding time  $t_{hold}$ . This step represents the fully loaded condition of the engine. In this stage, the material experiences stress relaxation which can be seen in figure 3.5 as a drop in compressive stress from Point B to C.

**Sequence C→D:** After the set holding time  $t_{hold}$ , the specimen is started to cool by reducing the heat input from  $T_{max}$  to  $T_{min}$  at a constant cooling rate mentioned under section 3. And the strain is reduced to a relative value of  $-(1 - \gamma)\alpha\{(T_{max} - T_{min})\}$  obtained from equation 3.1. This unloads the compressive stresses elastically. On further cooling by blowing air at 7 V, the material is loaded elastically until plasticity develops in tension followed by some hardening until Point D as seen in figure 3.4.

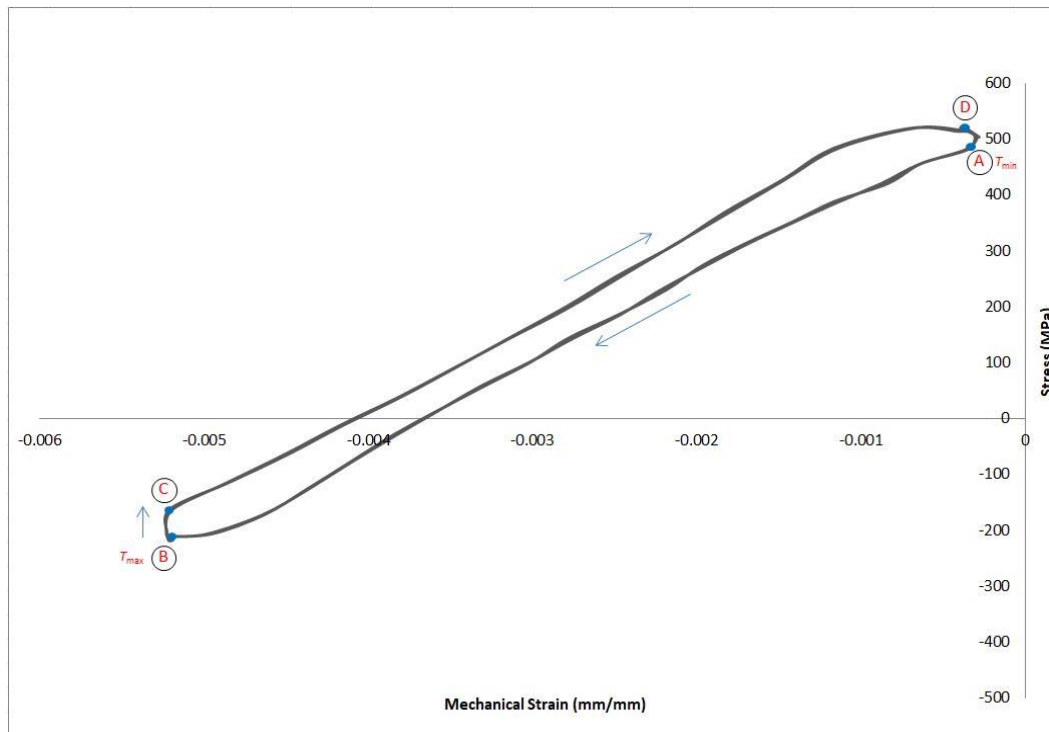


Figure 3.5 Typical mid-life hysteresis for out-of-phase partial constraint *TMF* test

**Sequence  $D \rightarrow A$ :** The temperature and strain are held constant at  $T_{\min}$  for a longer holding time. This longer hold time is provided at  $T_{\min}$  to allow for the measured specimen temperature value to reach the set point value as can be seen in figure 3.4. During the holding time at  $T_{\min}$  no significant stress relaxation is seen because of low temperature and the maximum tensile stress is reached at  $T_{\min}$  (see figure 3.5).

This sequence *ABCD*A constitutes of a single *TMF* cycle. This sequence repeated is for all test series until the test stop criterion (explained later in the chapter) is reached. Using the general *TMF* test procedure, the three test series performed in this study and the reasons for varying the parameters are elaborated below. The development of stress-strain hysteresis loop for the three test series is explained in chapter 4 along with the results.

### ***TMF* Test Series Benchmark Ranking**

This test series is performed as a benchmarking *TMF* test to compare and rank the performance of SiMo 5.10 (A1&2), SiMo4.05 (B1) and SiMoNi (C1) materials by investigating effect of thermal cycling and high temperature. The Benchmark *TMF* test procedure is designed by cycling the temperature between 50 °C ( $T_{\min}$ ) and 550 °C ( $T_{\max}$ ) with a holding time  $t_{\text{hold}}$  of 30 s (at  $T_{\max}$ ). These temperatures were chosen according to the loaded and unloaded conditions respectively of an exhaust manifold during the start-stop cycle of an engine in operation as mentioned in chapter 1. The

strain set-points for partial constrain condition in this case for SiMo 5.10 is calculated by equation 3.1 as:

$$\begin{aligned}\epsilon_{net} &= (1 - \gamma)\alpha^c\{(T_{max} - T_{min})\} \\ &= (1 - 0.75) \times 13.5 \times 10^{-6}\{(550 - 50)\} \\ \epsilon_{net} &= 1.7 \times 10^{-3}\end{aligned}$$

### TMF Test Series with $T_{min}$ 150 °C

The procedure for TMF test with  $T_{min}$  150 °C is designed by cycling the temperature between 150 °C ( $T_{min}$ ) and 550 °C ( $T_{max}$ ) with  $t_{hold}$  of 30 s to compare the TMF performance of heat-treated (A1) and non-heat-treated (A4). The  $T_{min}$  is raised from 50 °C to 150 °C for two reasons – first, because while A1 has better mechanical properties at room temperature relative to A4, at temperatures above 150 °C, they have comparable properties. Second, and more importantly, because 150 °C is better representative of  $T_{min}$  encountered in service conditions.

### TMF Test Series effect of $t_{hold}$

This test series is performed to study the effect of long holding time on SiMo 5.10 (A1) and SiMo 4.05 (B1) by investigating their stress relaxation properties. The TMF test is designed by cycling the temperature between 50 °C ( $T_{min}$ ) and 550 °C ( $T_{max}$ ) with a long holding time  $t_{hold}$  of 600 s. The in-service thermal cycle of an engine involves prolonged holding times at both  $T_{min}$  and  $T_{max}$ .

Table 3.2 TMF test series, their respective parameter and materials tested in this study

TMF Test series Material Code Tested	TMF Test Parameters		
	$T_{max}$ °C	$T_{min}$ °C	$t_{hold}$ s
Test series 1: Benchmark test A1 to A3, B1, C1	550	50	30
Test series 2: With $T_{min}$ 150 °C A1 to A2 and A4	550	150	30
Test series 3: Effect of $t_{hold}$ A1 and B1	550	50	600

---

<sup>c</sup>  $\alpha$  is calculated as  $13.5 \times 10^{-6} K^{-1}$  for SiMo 5.10 (dealt later in the chapter)

### 3.4. Coefficient of Thermal Expansion (CTE)

The coefficient of thermal expansion of each specimen material is obtained as the slope of the plot between the measured axial strain of free expansion due to heating as a function of temperature. As seen in section 3.3, the programmed relative set-point value for net strain is a function of  $\alpha$ , since the thermal strain and thereby the mechanical strain is a function of  $\alpha$ . Hence, the CTE value is an important parameter in TMF testing. The following steps are followed in obtaining the coefficient of thermal expansion.

**Step 1:** The specimen is placed inside both grips and clamped. The machine set to load control and the load value is set to zero as the clamping action raises the load in the specimen.

**Step 2:** Next, the specimen is heated gradually from room temperature to 600 °C in 120 s. Correspondingly, the total axial strain of the specimen is measured. The procedure to obtain the CTE value is performed under no load conditions. Therefore, the set-point for the force command channel is programmed to zero throughout the procedure.

**Step 3:** The temperature at 600 °C and the corresponding strain are held constant for a holding time of 30 s so that they stabilize.

**Step 4:** After a holding time of 30 s, the specimen is cooled by reducing the heat input from 600 °C to room temperature in a period of 120 s. The corresponding strain is also measured in the cooling cycle. There is no external cooling provided at this stage.

Initially, the coefficient of thermal expansion was obtained by measuring the strain while heating an unclamped (upper grip) specimen from room temperature to 600 °C, thus in free expansion. This led to a 5% error in the obtained CTE values for test series 1 for materials A2, B1 and C1. Later, for test series 2 and 3, CTE values were obtained by clamping the specimen with both grips as this led to more consistent value for  $\alpha$  due to uniform heating of the gauge section. Table 3.3 tabulates the CTE and corresponding net strain set-points obtained. The CTE procedure was followed before starting the TMF program for all the tests to check for the consistency of  $\alpha$  values; thereby ensuring correct operation of the thermocouples and extensometer.

Table 3.3 CTE and  $\epsilon_{net}$  values used in this study

Material → Code → Batch →		Thermal expansion Coefficient <sup>d</sup> $\alpha$ ( $\times 10^{-6} K^{-1}$ ) Net strain <sup>e</sup> $\epsilon_{net}$ (-) ( $\times 10^{-3}$ )					
		SiMo5.10				SiMo4.05	SiMoNi
		A1 ( D )	A2 ( X )	A3 (Kalra)	A4 (No HT)	B1 -	C1 -
<b>TMF test condition ↓</b>							
<b>Test Series 1: Benchmarking</b> $T_{min} = 50\text{ }^{\circ}\text{C}$ ; $t_{hold} = 30\text{ s}$	13.5 1.7	12.8 1.60	13.5 1.7	—	12.5 1.56	12.8 1.61	
<b>Tet Series 2: With <math>T_{min} 150\text{ }^{\circ}\text{C}</math></b> $T_{min} = 150\text{ }^{\circ}\text{C}$ ; $t_{hold} = 30\text{ s}$	13.5 1.35	13.6 1.36	—	13.5 1.35	—	—	
<b>Test Series 3: Effect of <math>t_{hold}</math></b> $T_{min} = 50\text{ }^{\circ}\text{C}$ ; $t_{hold} = 600\text{ s}$	13.5 1.7	—	—	—	13.1 1.63	—	

### 3.5. TMF Test Termination Criterion

A TMF test should run uninterrupted until termination which is generally characterized by the complete separation of the specimen [34]. In this case of complete separation, the number of load cycles till failure,  $N_f$  is the TMF lifetime of the specimen. However, the termination of the TMF before complete failure is preferred; especially in the case of brittle materials as it can damage the extensometer. Therefore for strain controlled TMF tests, the termination criterion is a drop in the maximum force value developed during the test by a predetermined percentage. Based on the requirements, the magnitude of this drop can be between 5% and 50% of the maximum force developed [35].

It should be explained here that the drop in the maximum force developed during the test is due to the development of a macro crack. However, the drop in the maximum force is not always consistent. It is found that this inconsistency is due to the fact that often the asymmetrical fatigue crack initiates at a random position along the circumference with respect to the position of the extensometer [20]. Ghodrati [20] was able to reduce the influence of the extensometer position on TMF lifetime, by defining a 10% drop in maximum force developed during the TMF test as the termination criterion. The number of cycles for the maximum force to drop by 10% is denoted by  $N_{10}$  and is employed as the TMF failure criterion for the tests performed in this study.

<sup>d</sup> Measured values

<sup>e</sup> Relative net strain values used in the TMF program calculated using equation (3.1)

Zafeiropoulos [27] and Kalra [4] have successfully used the  $M_{10}$  failure criterion for testing *TMF* for SiMo ductile cast irons.

### 3.6. Paris Lifetime Calculations

As mentioned earlier in chapter 2, it is possible to numerically estimate *TMF* lifetimes by calculating the stress intensity range and correlating it to *TMF* crack growth through the Paris equation

$$\frac{da}{dN} = C(\Delta K_I)^m,$$

where  $a$  is the crack length,  $N$  is the number of *TMF* cycles and  $\Delta K_I$  is the stress intensity range.  $C$  and  $m$  are material dependent Paris parameters. Building upon the previous work [4] [36] performed on calculating numerical *TMF* lifetimes, the notch depth of the specimen is used as the initial crack length as the cracks are assumed to initiate from the notch. The  $K$  solution for a cylindrical specimen containing a circumferential notch as seen below is a complex solution to be analytically integrated. Therefore, the lifetime is calculated by numerical integration.

$$K_I = \sigma\sqrt{\pi a} \frac{1}{(1-\frac{a}{r})^{3/4}} \{1.22 - 1.302 \left(\frac{a}{r}\right) + 0.988\left(\frac{a}{r}\right)^2 - 0.308\left(\frac{a}{r}\right)^3\} \quad (4.1)$$

Where  $K_I$  is the stress intensity factor for mode I loading condition,  $a$  is the crack length and  $r$  is the radius of the specimen gauge length. It should be mentioned here that all the previous work done on calculating the numerical *TMF* lifetimes was performed using specimens with various notch depths. This was necessary to obtain the appropriate Paris parameters to correlate experimental lifetimes with calculated lifetime. For reasons mentioned earlier only a single notch depth (0.15 mm) was used in this study. Using only a single notch depth it is not possible to predict the lifetime with certainty as it leads to infinite combinations of  $C$  and  $m$  values. Therefore,  $C$  and  $m$  values used in this study were obtained from the work performed by Kalra [4] on material SiMo 4.10 which has similar nominal composition to that of SiMo 5.10 (see table 3.1).

Kalra [4] found that the Paris parameter  $C$  varied linearly with mechanical strain range whereas the parameter  $m$  remained constant. Using equation 2.6, the Paris parameter  $C$  was calculated for the SiMo 5.10 material for benchmark ranking *TMF* tests and *TMF* test with  $T_{min}$  150 °C.

**Table 3.4 Calculated Paris parameters benchmark ranking and  $T_{min}$  150 °C TMF tests [4]**

Temperature Range ( $T_{min} - T_{max}$ ) ( °C) for SiMo5.1	Mechanical Strain Range	Paris Constants	
		$C$	$m$
50 °C – 550 °C	0.0051	1.20E-10	3.6
150 °C – 550 °C	0.0045	1.50E-10	3.6

### 3.7. Material Characterization

The material characterization techniques used to investigate the microstructure and the *TMF* crack paths are explained in this section.

### 3.8. Optical Microscopy

A Leica DFC 320 optical microscope is used to make micrographs of the specimens. A cross section of gauge section of the dog-bone specimen is cut using a circular laboratory saw. The cut cylindrical specimen is cold mounted in a resin. Since hot mounting reaches 500 °C, it was avoided to prevent thermal loading of the specimen close to  $T_{max}$  of *TMF* testing [27]. The mounted specimens are prepared metallographically. Special attention is paid to the metallographic preparation of cast iron specimens. The softer graphitic phase poses a risk of loosening from the harder matrix phase during grinding operation.

For this reason, the specimens are prepared using a specific procedure as mentioned in [27]. To obtain a flat surface and at the same time retain the graphitic phase in the specimen, the number of steps in the grinding stage is minimized (320 grit for coarse and 800 grit for fine). After the grinding stage, the polishing stages of 6 $\mu$ m, 3  $\mu$ m and 1  $\mu$ m were performed for 3 minutes each to remove the final surface scratches. The un-etched sample when observed under the optical microscope shows the matrix with graphite phases embedded in it. However, it does not provide any information on the porosity as the specimens are extracted from Y-blocks and not from the exhaust manifold itself [27]. The polished specimens are etched to observe the microstructure under the optical microscopes using magnifications between 10X and 100X. Etching with 1-3% Nital solution for 15 s [27] reveals clearly the grain boundaries and the molybdenum carbide phases.

A Keyence VHX-5000 digital microscope is used to measure information regarding the graphite distribution, nodule size and nodularity. The image is focused and “auto area measurement” option is selected under which the “dark area” option is selected so that

the microscope can detect the graphite particles. On clicking start measure, results are shown. Select add measures to include 'equivalent circular diameter' and 'circularity', options which provides the nodule size and nodularity of the graphite particles. Nodularity is calculated as the ratio of the area fraction exceeding a critical curvature to the total area fraction of graphite.

### **3.9. Scanning Electron Microscopy**

The fracture surfaces obtained by complete failure of the specimens during TMF testing were observed using a Scanning Electron Microscope (SEM). The SEM used in this study is JEOL JSM 5600F in the material characterization lab. The fracture surfaces of the specimens were obtained by carefully clamping one half of the broken specimen in the circular laboratory saw and cutting it transversely. Care is taken here to cut the specimen in the gauge length far away from the fracture surface with the intention of keeping it intact. The cut fracture surface is first cleaned in an ultrasonic bath with ethanol and then acetone for a period of 5 minutes each. It is very important that the cleaned specimens are completely dried before being observed in the SEM.

The vacuum chamber in the SEM is evacuated initially before the specimen is introduced. Care is taken not to damage the electron gun in this process. After the introduction of specimen, the chamber is vacuumized. Optimum magnification, contrast and brightness are used to view the image. At higher magnifications, correction for astigmatism is performed to obtain a clear image. Good focus to depth ratio is obtained by using large working distance (WD). This is necessary to obtain good images of the fracture surfaces as they are very rough and hence difficult to focus the peaks and valleys.

### **3.10. Vickers Hardness Testing**

The hardness measurements are obtained by DuraScan 10 G5. The specimens are prepared in a similar method as for optical microscopy. The sample to be tested is placed in holder. Care is taken that the material surface is flat to obtain accurate measurements. The hardness values are generated by the setup as a function of the diagonal lengths of the indents created. Both micro and macro-hardness values were tested in this study. A HV0.2 load is used for measuring micro-hardness and a HV 1 load is used for measuring macro-hardness values.

## 4. Results and discussion

The test matrix provides an overview of the *TMF* test series performed, as described in section 3.3 on the included materials, and their respective average *TMF* lifetimes, average stress ranges,  $\Delta\sigma$  and average peak stresses,  $\sigma_{\max}$  that developed during each test (Refer Appendix A). The mechanical strain range,  $\Delta\varepsilon_{\text{mech}}$  is calculated for the three test series using equations 2.3 and 2.4.

Table 4.1 Test Matrix

		Average $N_{10} \pm \text{St.Dev.}$ Average $\Delta\sigma \pm \text{St.Dev. (MPa)}$ Average $\sigma_{\max} \pm \text{St.Dev. (MPa)}$					
Material →		SiMo5.10				SiMo4.05	SiMoNi
<i>TMF</i> test <sup>f</sup>	Code →	A1	A2	A3 <sup>g</sup>	A4	B1	C1
condition ↓ $\Delta\varepsilon_{\text{mech}}$	Batch →	(D)	(X)	-	(N)	-	-
<b>Test Series 1: Benchmark Ranking</b> $T_{\min} = 50 \text{ }^{\circ}\text{C}$ ; $t_{\text{hold}} = 30 \text{ s}$ ; 0.0051		<b>107 ± 7</b> 659 ± 10 473 ± 1	<b>91 ± 2</b> 664 ± 2 475 ± 1	<b>168 ± 9</b> 654 ± 10 484 ± 23	—	<b>61 ± 10</b> 689 ± 3 491 ± 1	<b>85 ± 22</b> 741 ± 1 525 ± 3
<b>Tet Series 2: Effect of <math>T_{\min}</math></b> $T_{\min} = 150 \text{ }^{\circ}\text{C}$ ; $t_{\text{hold}} = 30 \text{ s}$ ; 0.0045		<b>97 ± 12</b> 596 ± 8 445 ± 9	<b>120 ± 32</b> 588 ± 6 440 ± 5	—	<b>194 ± 24</b> 606 ± 3 450 ± 4	—	—
<b>Test Series 3: Effect of Stress relaxation</b> $T_{\min} = 50 \text{ }^{\circ}\text{C}$ ; $t_{\text{hold}} = 600 \text{ s}$ ; 0.0051		<b>28 ± 9</b> 666 ± 3 491 ± 12	—	—	—	<b>31 ± 3</b> 672 ± 11 483 ± 1	—

### 4.1. *TMF* Results – Lifetimes and Stress-Strain development

#### *TMF* Test Series Benchmark Ranking

The test series 1, performed as a benchmark test to rank of all the included materials – SiMo 5.10 (A1&2), SiMo 4.05 (B1) and SiMoNi (C1) showed that the average *TMF*

<sup>f</sup> For all tests: notch depth = 0.15 mm,  $T_{\max} = 550 \text{ }^{\circ}\text{C}$ , with a number of three replicate tests.

<sup>g</sup> Results listed of on material A3 (SiMo 4.10) were obtained in previous work [4], for material with a nominal composition similar to materials A1, A2 and A4 (see table 3.1).

lifetimes  $N_{10}$  obtained are comparable. The highest average lifetime  $N_{10}$  is found to be about 100 cycles for SiMo 5.10 (both A1 and A2) while B1 has the lowest average  $N_{10}$  of about 60 cycles. C1 with an average  $N_{10}$  of 85 cycles is situated in between. The average stress ranges and peak stresses that developed during test series 1 for material A1 and A2 are similar. Material B1 and C1 showed relatively higher average stress ranges of about 690 MPa and 741 MPa, respectively.

Figures 4.1, 4.2 and 4.3 show the hysteresis loop that developed for A2, B1 and C1 respectively during test series 1 as explained in section 3.3. Initially, the material is heated from room temperature to 50 °C ( $T_{min}$ ) under free expansion. Since the partial constraint is applied at  $T_{min}$  and at zero stress, the first *TMF* cycle produces a large compressive plasticity. It can be seen from the figures, that as the number of *TMF* cycles increases, a mean tensile stress builds up. This is due to the fact that the material has lower yield strength in compression at high temperature than in tension at lower temperature. The mechanical strain range calculated for test series 1 (see table 4.1) as  $5.1 \cdot 10^{-3}$ . The plastic strain range of the material is given by the width of the hysteresis loop. It can be seen from the figures that initially, as the number of *TMF* cycles increases, the width of the hysteresis loop reduces indicating an increase in strength due to the mechanism of cyclic strain hardening [20].

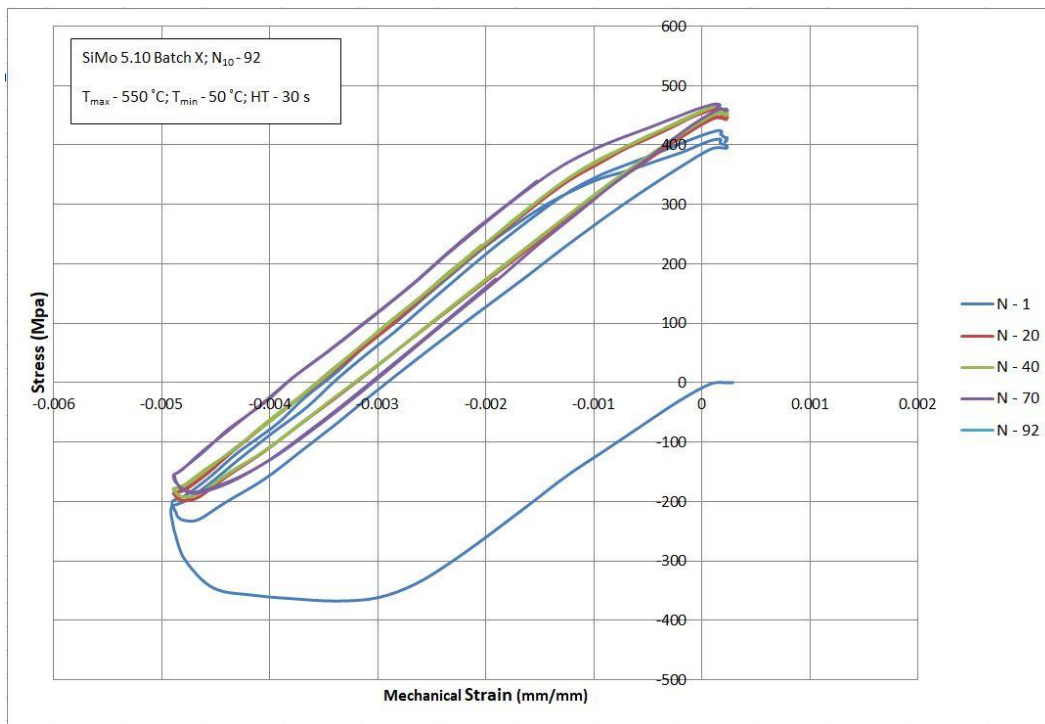


Figure 4.1 Stress-mechanical strain hysteresis loop for TMF test series 1 for A2

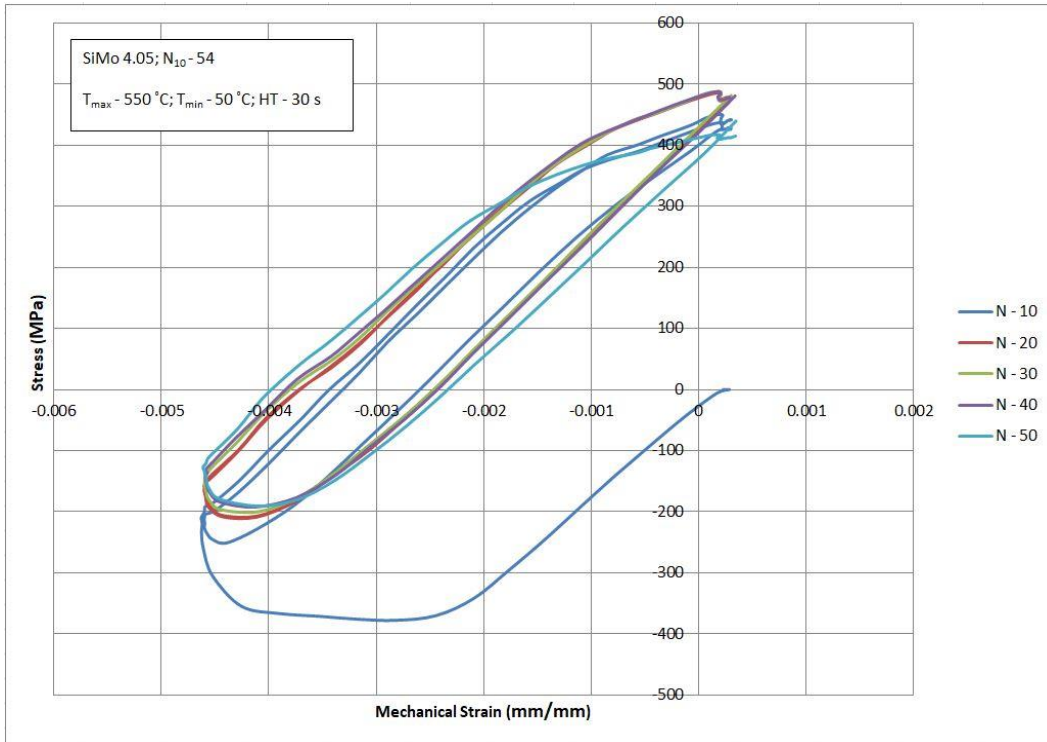


Figure 4.2 Stress-mechanical strain hysteresis loop for *TMF* test series 1 for B1

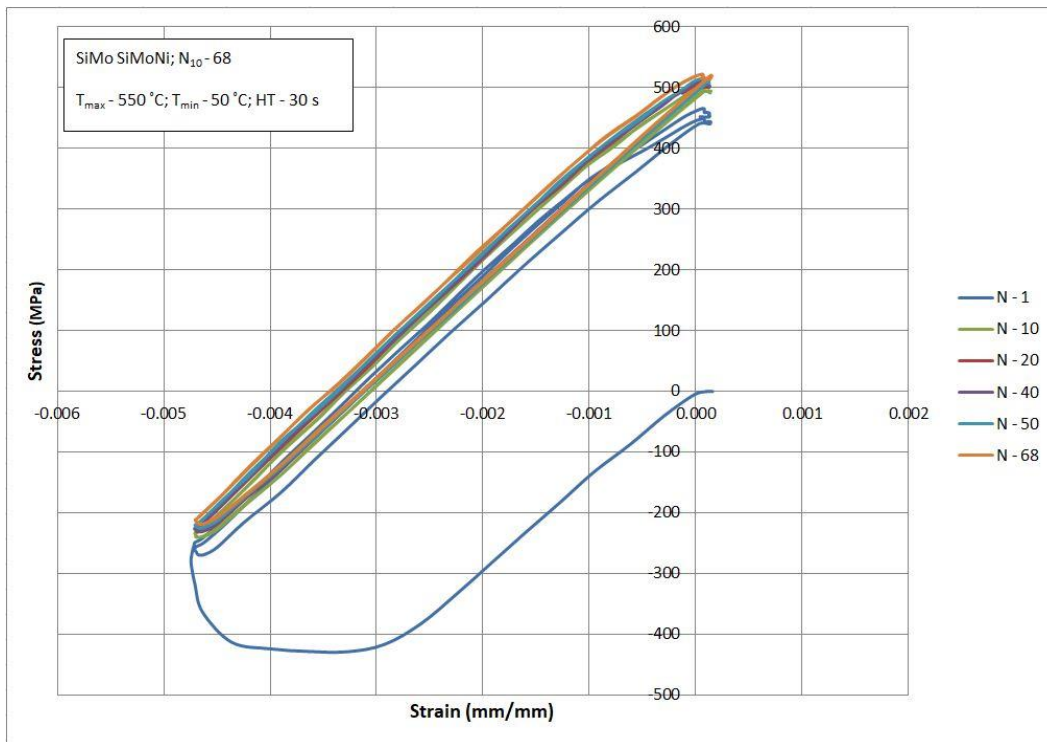


Figure 4.3 Stress-mechanical strain hysteresis loop for *TMF* test series 1 for C1

This causes the hysteresis loop to “climb” in the tensile direction up to a maximum peak stress value which in case of A2, B1 and C1 is about 475, 490 and 525 MPa respectively. A further increase in *TMF* cycles leads to softening due to the growth of a dominant macroscopic crack. This causes a drop in the peak stresses until complete failure in the case of A2 and B1. The lower average lifetime of B1 compared to A2 and C1 can be attributed to its high cyclic plasticity. In the case of C1, it can be seen from figure 4.4 that the plastic strain range remains almost constant throughout the *TMF* cycling and there is no drop in  $\sigma_{max}$  before complete failure. The failure mechanism of C1 is further dealt with in chapter 4.2.

### TMF Test Series with $T_{min}$ 150 °C

The *TMF* performance of heat-treated and non-heat-treated SiMo 5.10 is compared by test series 2, performed as mentioned in section 3.3. It can be seen from table 4.1 that non-heat-treated SiMo 5.10 shows better *TMF* performance than its heat-treated equivalent with an average  $N_{10}$  of about 194 and 110 cycles respectively. A1, A2 and A4 showed development of similar stress ranges during the *TMF* test. There is a 10% decrease in stress and strain range levels in the direction of test series from 1 to 2 due to an increase in  $T_{min}$  from 50 °C to 150 °C. This shows an increase in average  $N_{10}$  for material A2. However, the decrease in average  $N_{10}$  for material A1 is counter intuitive.

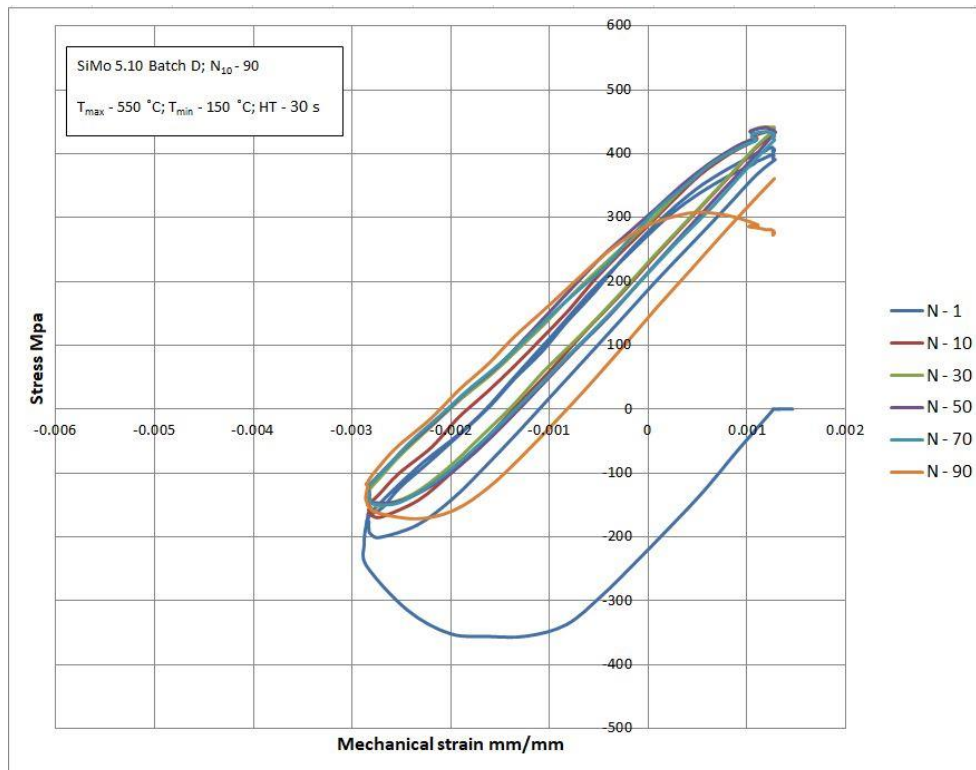


Figure 4.4 Stress-mechanical strain hysteresis loop for *TMF* test series 2 for A1

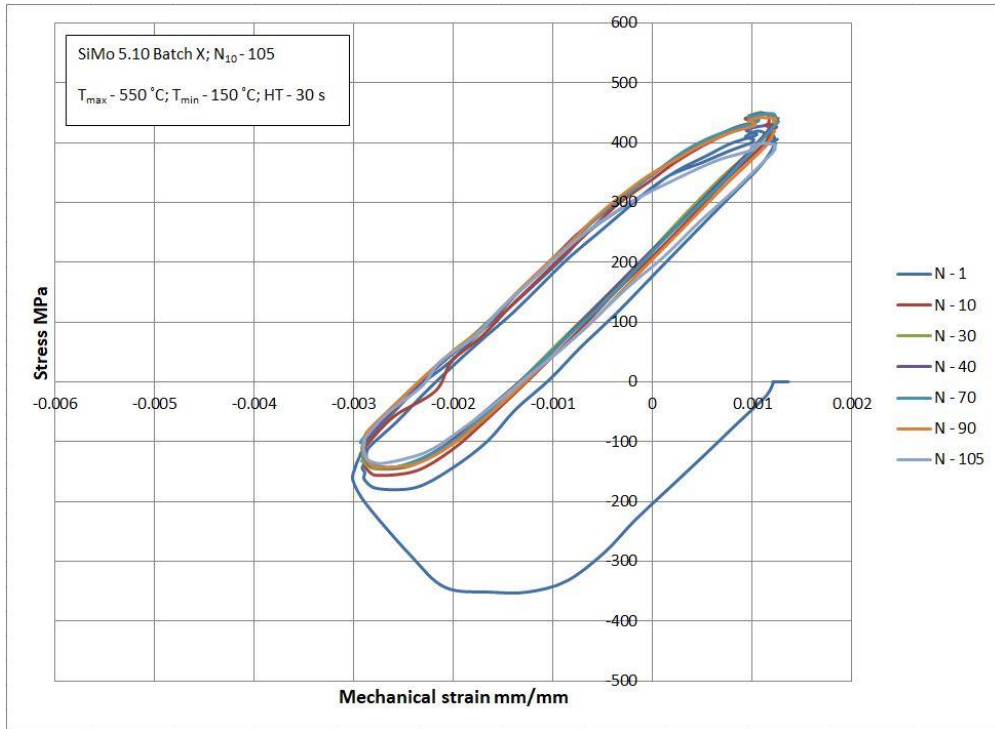


Figure 4.5 Stress-mechanical strain hysteresis loop for TMF test series 2 for A2

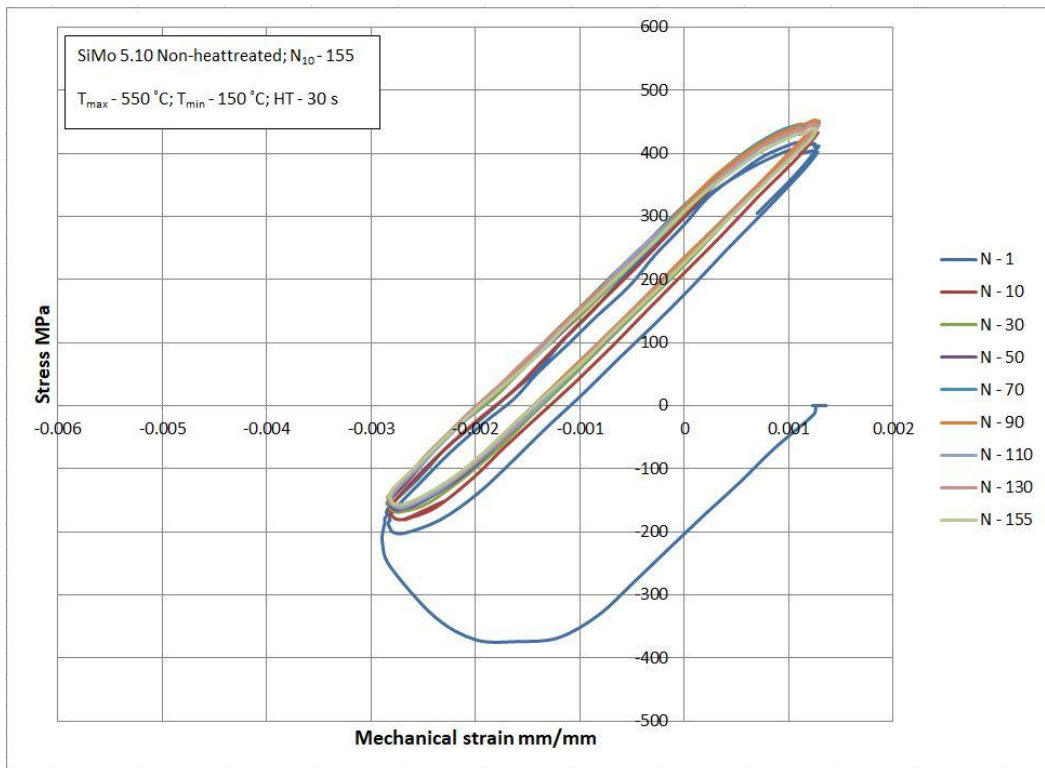


Figure 4.6 Stress-mechanical strain hysteresis loop for TMF test series 2 for A4

The hysteresis loop development during *TMF* test series 2 for materials A1 and A2 as seen in figures 4.4 and 4.5 respectively is similar to the principle explained earlier. However, it can be seen from the figures that the first *TMF* cycle produces less plasticity in compression relative to test series 1. This is because the partial constraint condition is applied and the material is loaded only from a  $T_{\min}$  of 150 °C as opposed to 50 °C in the test series 1. The relatively lower stresses developed during compression is compensated in tensile direction. Therefore, the mean stress build up in tension is lesser compared to test series 1. By increasing the  $T_{\min}$ , thermal strain developed in the material reduces; thereby decreasing the mechanical strain range. This leads to a marginally higher average lifetime for A2 compared to test series 1. Figure 4.6 shows the stress-strain hysteresis loop for material A4. It can be seen that the lower cyclic plasticity that develops compared to A1 and A2 contributes to the higher average *TMF* lifetime.

As mentioned earlier, two batches of heat-treated SiMo 5.10 material were tested since the batch D was initially mistaken to be non-heat-treated specimens. Changes in casting conditions in the form of batches can cause subtle differences in specimens (material chemistry, microstructures) which can affect the *TMF* performance. However, as can be seen from table 4.1, the *TMF* performance of A1 and A2 in test series 1 and 2 are comparable; and hence show that the casting process is reproducible.

#### ***TMF Test Series effect of $t_{hold}$***

The main aim of test series 3 is to investigate the effect of the holding time on the *TMF* performance of materials A1 and B1. The test procedure is conducted according to section 3.3 and *TMF* lifetime results are compared to results of test series 1. For the prolonged holding time, a significant decrease in average lifetime is found for both materials A1 and B1, showing lifetime reductions of 49% and 72%, respectively. Noticeably, the stress and strain range values were similar for both holding times. The reason for the reduced lifetimes can be explained by considering the *TMF* crack growth to be a balance between the 'crack driving forces' (stress and strain ranges) and the materials 'resistance' to crack growth; and the prolonged holding time seems to reduce this resistance.

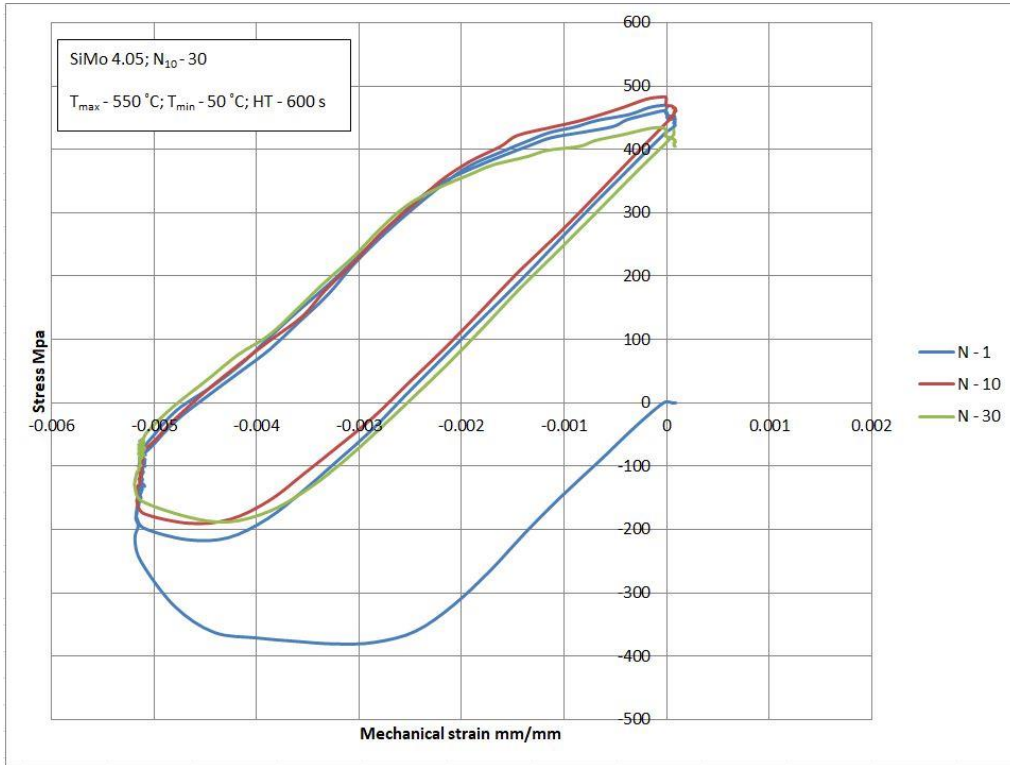


Figure 4.7 Stress-mechanical strain hysteresis loop for long hold time TMF test for SiMo4.05

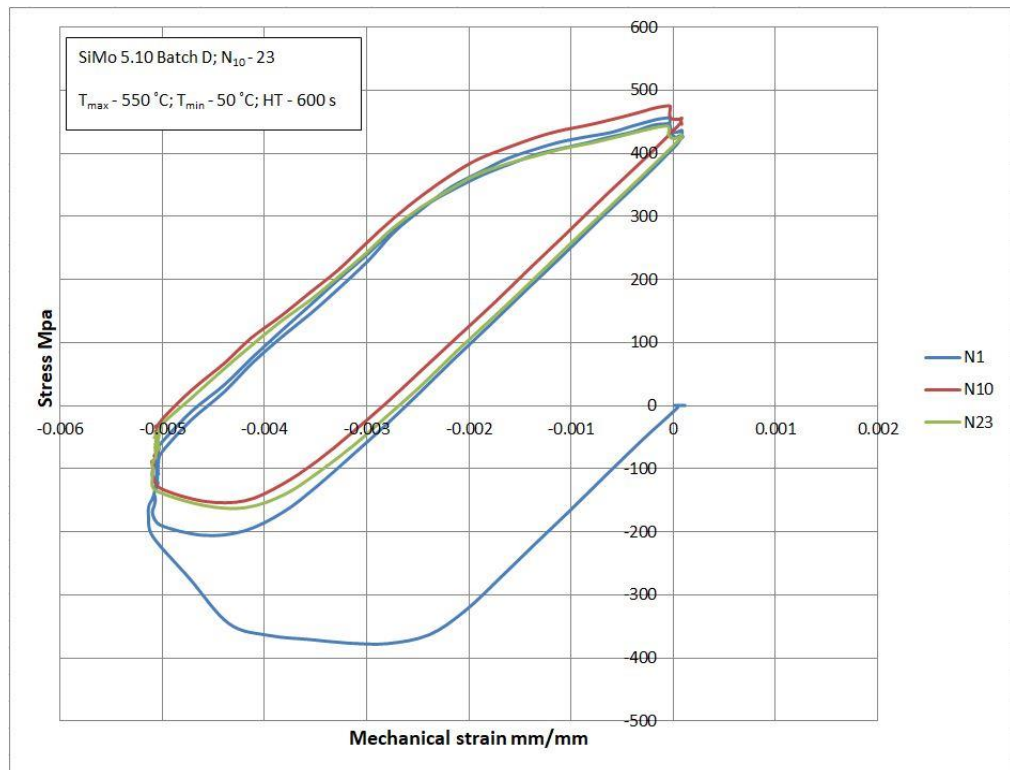


Figure 4.8 Stress-mechanical strain hysteresis loop for TMF test series 3 for SiMo5.10

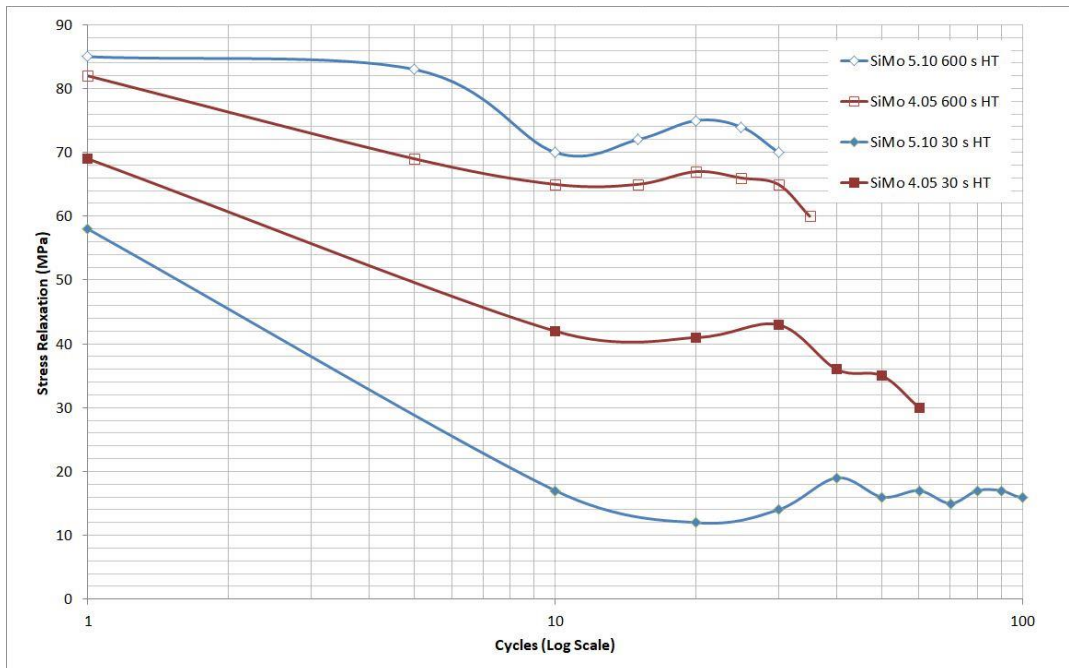


Figure 4.9 Evolution of stress relaxation as a function of TMF cycles for A1 and B1 with 30 s and 600 s holding time

The stress-strain hysteresis loop development during test series 3 is similar to test series 1 except for two apparent observations as seen in figures 4.7 and 4.8. The hysteresis loops of test series 3 shows relatively more stress relaxation, due to a longer  $t_{\text{hold}}$ , and higher cyclic plastic strain ranges. The stress relaxation causes the compressive stresses to decrease during  $t_{\text{hold}}$ . Hence, the cooling cycle begins from a relatively lower compressive stress resulting in higher tensile peak stresses as the *TMF* cycles progress.

Figure 4.8 shows the evolution of stress relaxation with the number of cycles for materials A1 and B1 for both the holding times. The stress relaxation is calculated as the reduction in compressive stress at 550 °C due to the holding time. At short  $t_{\text{hold}}$  of 30 s, the higher stress relaxation of B1 can attribute for its higher peak stresses in test series 1 (see table 4.1) compared to A1. However, at long  $t_{\text{hold}}$  of 600 s in test series 3, A1 shows relatively higher stress relaxation resulting in higher peak stresses in A1 than in B1.

While increasing  $t_{\text{hold}}$  increases cyclic plasticity, it can be seen from the figures 4.6 and 4.7 that there is very little or no strain hardening occurring with progressing *TMF* cycles unlike test series 1. This could be due to fact that a dominant macroscopic crack starts growing after a few initial *TMF* cycles thus supporting the hypothesis that the 'resistance' to crack growth for materials A1 and B1 reduces with increase in  $t_{\text{hold}}$ . The high cyclic plasticity also contributes to the large drop in lifetimes.

## 4.2. Effect of Notching in SiMoNi – Fracture Toughness vs Fatigue

As mentioned in chapter 1, previously performed TMF tests on SiMoNi (C1) material showed very low lifetime and large scatter in the results obtained. These *TMF* tests were conducted on notched specimens with 0.15 mm notch depth under total constraint conditions. It was seen earlier in this chapter that C1 fails suddenly at the maximum of the peak stress evolved with increasing number of cycles during test series 1. This can be seen in figure 4.3 and also in figure 4.9.

The fatigue crack growth in C1 is numerically calculated using Paris equation 2.4. Since there is no crack closure for small cracks, hence  $\Delta K_I = K_{max} - K_{min}$ . Therefore using the Paris parameters  $C = 3.3E-11$  and  $m = 3.58$  in the case of disregarding crack closure [4] and assuming the initial crack length is equal to the notch depth 0.15 mm, the fatigue crack growth for SiMoNi can be calculated.

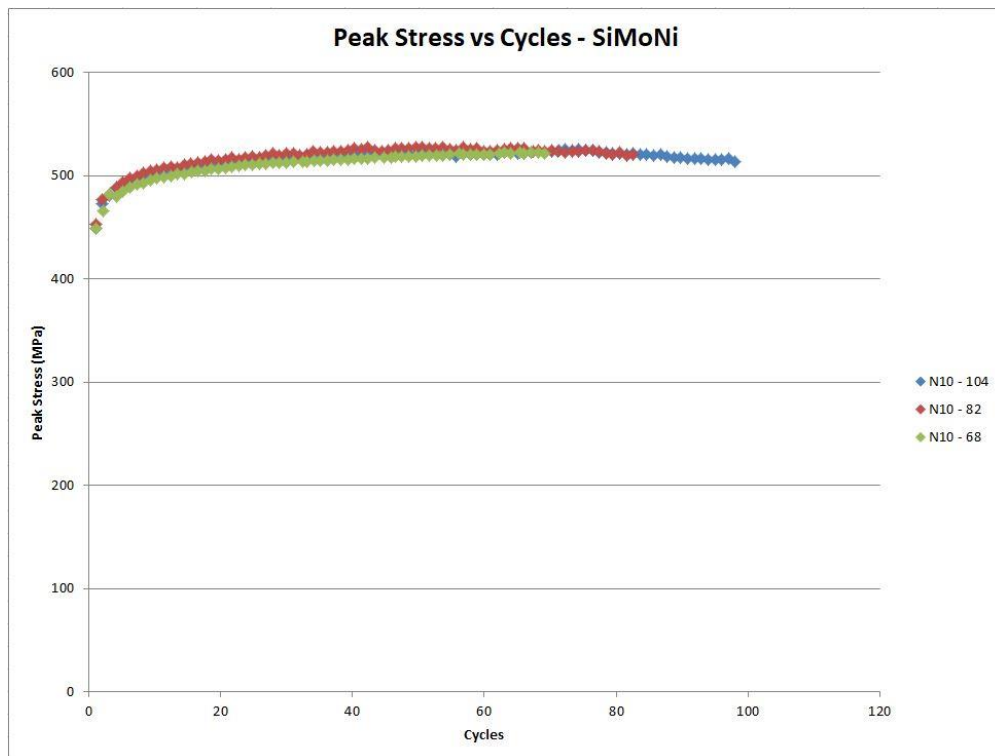


Figure 4.10 Development of Peak stresses during TMF test series 1 for material C1

It can be seen that the final crack extension in C1 during *TMF* is about 238  $\mu\text{m}$ . The fatigue crack extension is also calculated using measuring the compliance of a cracked specimen. The decrease in stiffness due to crack growth is calculated by measuring the equivalent stiffness of the same specimen in the first and last cycle of a *TMF* test to

avoid any systematic errors and also errors in placing of the extensometer. Using Tada solution<sup>h</sup> the fatigue crack growth in C1 is calculated as 480  $\mu\text{m}$ .

Table 4.2 Calculation of fatigue crack growth in C1

<i>TMF</i> Test series: 1 data – SiMoNi (C1)				Paris Parameters		Crack extension	
$a_0$ ( $\mu\text{m}$ )	Average $\Delta\sigma \pm \text{S.D}$ (MPa)	Average $N_{10} \pm \text{S.D}$	$\Delta K_I$ ( $\text{MPa}\sqrt{\text{m}}$ )	$C$	$m$	$da/dN$ $\pm \text{S.D}$ ( $\mu\text{m}/\text{cycle}$ )	$a_c \pm \text{S.D}$ ( $\mu\text{m}$ )
150	$740 \pm 1$	$85 \pm 22$	18.39	3.3E-11	3.58	$1.10 \pm 0.005$	$238 \pm 12$

With these observations it can be seen that the amount of fatigue crack growth is very small and the material fails due to the fact the  $K_{Ic}$  is reached in quite early in the fatigue cycle. This explains the low average lifetimes in previously performed *TMF* tests. It can be hypothesized that in notched specimens initially, the blunt notch is closely surrounded by number of spherical graphite particles. Local stresses at the notch tip will not be as high as they would be at the tip of a real crack. Consequently fracture will not occur yet. After a few *TMF* cycles, a real crack initiates from the notch tip causing the stresses to become high enough to lead to fracture.

### 4.3. Paris Lifetime Calculations

Using the  $C$  and  $m$  values from table 3.4, and the procedure mentioned in section 3.6, the numerical estimate of *TMF* lifetimes were calculated for all the specimens of materials A1, A2 and A3 in test series 1 and 2 using a MATLAB program (Refer appendix D). The effect of batches is not recognized in the numerical *TMF* lifetime estimation and hence neglected here.

It can be seen from table 4.6 that while the experimental and calculated average  $N_{10}$  values show good agreement for test series 1, there is about 50% difference between the two in test series 2 for heat-treated SiMo 5.10. It should be noted that the  $C$  and  $m$  values were calculated using equation 2.6 [4] derived for different constraint levels at constant  $T_{\min}$  of 50 °C. Therefore, it is likely that the difference in the experimental and calculated values is due the fact that the *TMF* crack grows at  $T_{\min}$  150 °C test series 2.

---

<sup>h</sup> Appendix C

Table 4.6 Paris lifetime prediction for SiMo5.1 for *TMF* test series 1 and 2

Temperature Range ( $T_{min} - T_{max}$ ) (°C) Material	Peak Stress (MPa)	$\Delta\sigma$ (MPa)	$N_{10}$	Average $N_{10}$	$N_{10}$ (Paris)	Average $N_{10}$ (Paris)	Paris Parameters	
							$C$	$m$
50 °C – 550 °C (test series 1) SiMo 5.10 Heat-treated	472	670	114	100	103	103	2.10E-10	3.6
	469	667	108		105			
	473	656	100		102			
	478	663	92		98			
	477	665	90		97			
150 °C – 550 °C (test series 2) SiMo 5.10 Heat-treated	444	585	105	109	159	161	1.50E-10	3.6
	434	583	165		173			
	442	596	91		162			
	438	595	88		167			
	455	606	110		145			
	441	587	93		162			
150 °C – 550 °C (test series 2) SiMo 5.10 Non-heat-treated	446	602	246	193	156	151	1.50E-10	3.6
	450	605	180		151			
	454	610	155		146			

This shows the temperature dependency of Paris parameters and that the equation 2.6 cannot be applied universally for any constraint conditions applied by changing the temperature range. It is also interesting to see that according to the numerical estimates, a heat-treatment of SiMo 5.10 leads to a marginal increase in average  $N_{10}$  values due to a decrease in the peak stresses. However, it is seen that in reality it is the contrary. This supports the earlier discussion that the *TMF* lifetime is a balance between ‘crack driving forces’ and the inherent ‘resistance’ of the material. A heat-treatment seems to decrease this resistance of SiMo 5.10 as explained in the following chapter.

#### 4.4. Material Characterization

The microstructures for all the included materials are obtained as mentioned in section 3.3. Metallographic investigations show that all the materials exhibited a ferritic matrix with uniformly distributed graphite nodules as expected. Etching with 2% Nital revealed the grain boundaries and the present eutectic carbide phases. The carbide phases are found to be confined mostly near the grain boundaries. The Mo-rich phases are found as fine precipitates confined in the grain boundaries due to alloy segregation [21]. The eutectic carbides found in the microstructures are known to be of two types –  $M_6C$  and  $M_7C_3$  type [27] where M can be Fe, Si or Mo. These carbide phases are known to be stable up to the  $Ac_1$  temperatures of the material [17].

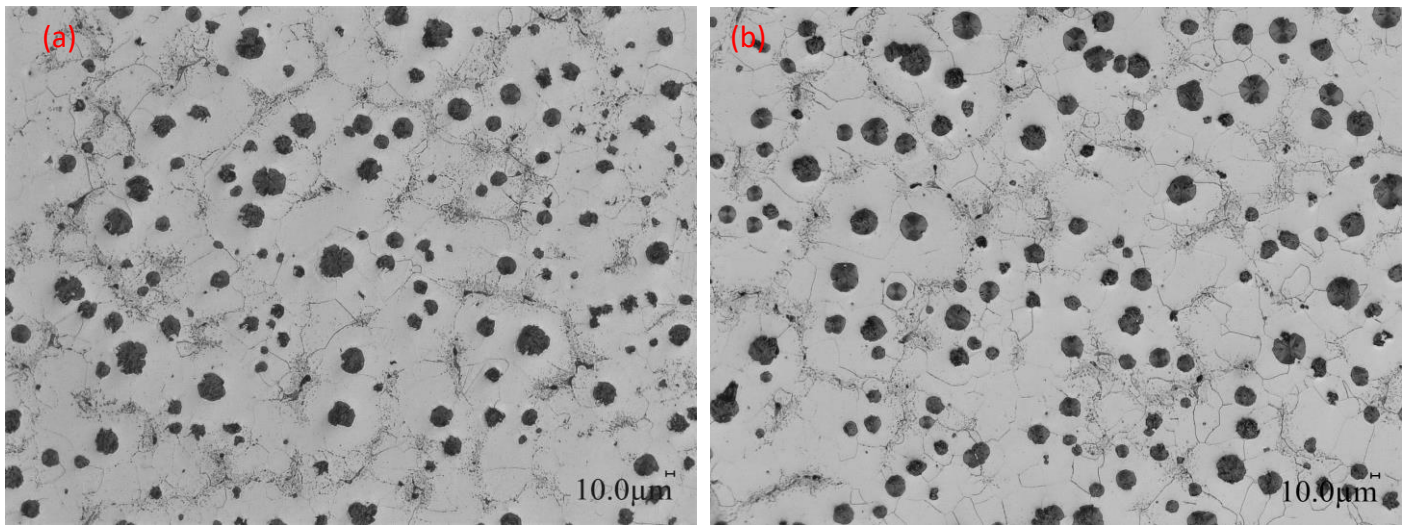


Figure 4.11 Microstructure of SiMo 5.10 a) Batch D b) Batch X

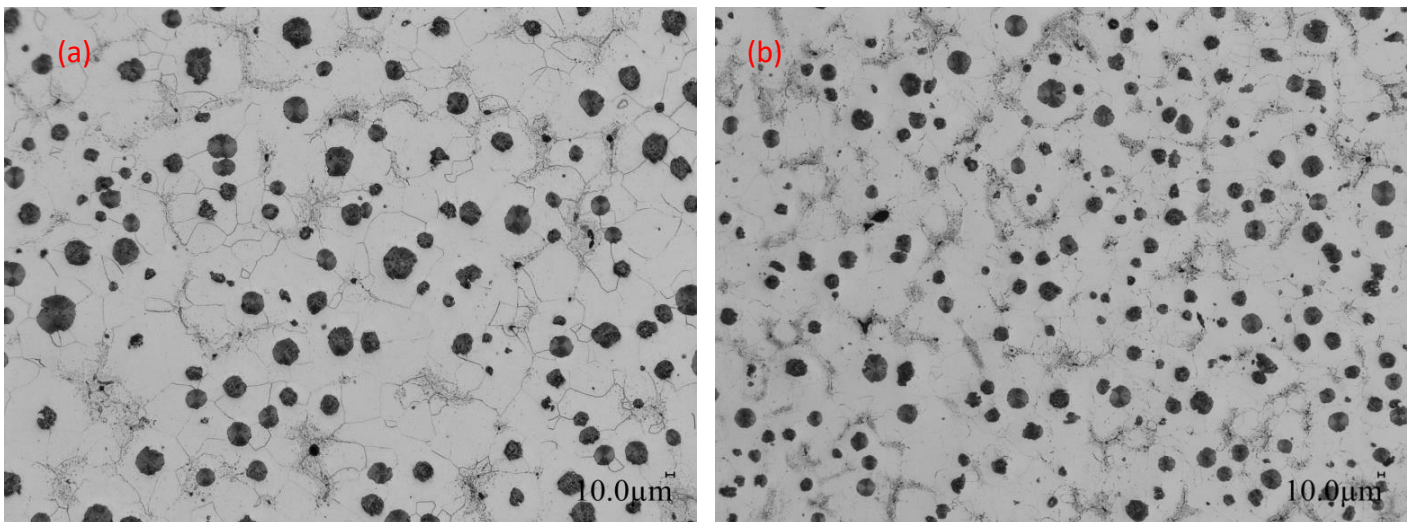


Figure 4.12 Microstructure of a) SiMoNi b) SiMo 4.05 cast iron

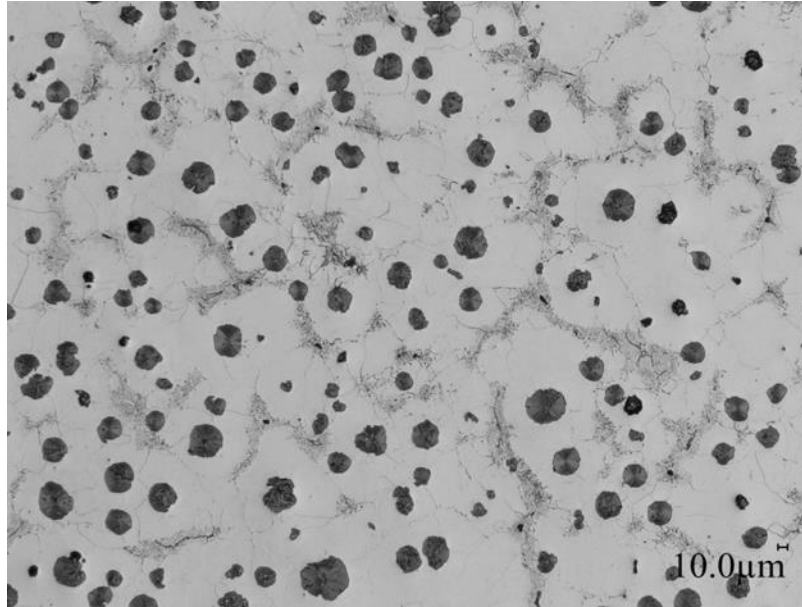


Figure 4.13 Microstructure of non-heat-treated SiMo 5.10 cast iron

Table 4.3 Graphite Particle data for the materials tested in this study

Material	Equivalent diameter $\pm$ S.D (um)	Nodularity $\pm$ S.D (-)	Area ratio (%)
A1	24 $\pm$ 6	0.8 $\pm$ 0.1	6.0
A2	22 $\pm$ 5	0.9 $\pm$ 0.1	7.5
A3	24 $\pm$ 7	0.7 $\pm$ 0.1	8.5
B1	25 $\pm$ 8	0.9 $\pm$ 0.1	8.5
C1	21 $\pm$ 6	0.7 $\pm$ 0.1	7.0

It can be seen from figure 4.11 and table 4.3 that the microstructure, graphite particle sizes and nodularity in both the batches of SiMo 5.10 (A1 and A2) are similar reiterating the fact that the casting process is reproducible. Figure 4.12 shows that a reduction in Mo content or by alloying with Ni in the case of SiMo 4.05 and SiMoNi respectively, does not change the microstructure significantly. From figures 4.10, 4.13 and table 4.3, it can be seen that there is no change in grain sizes and graphite particle sizes due to heat-treatment.

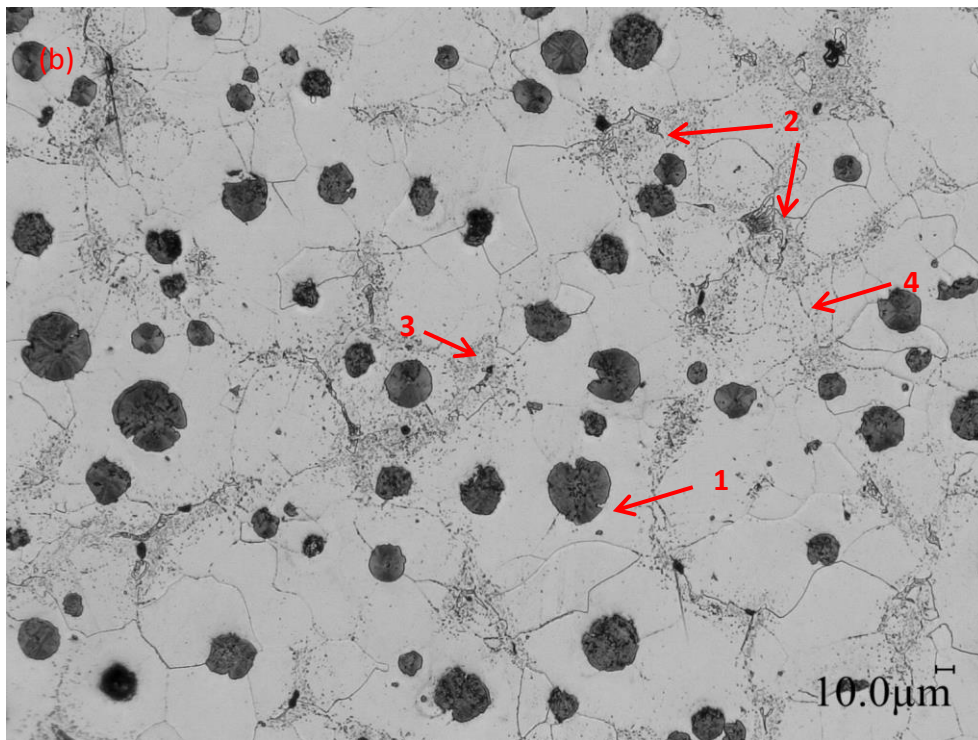
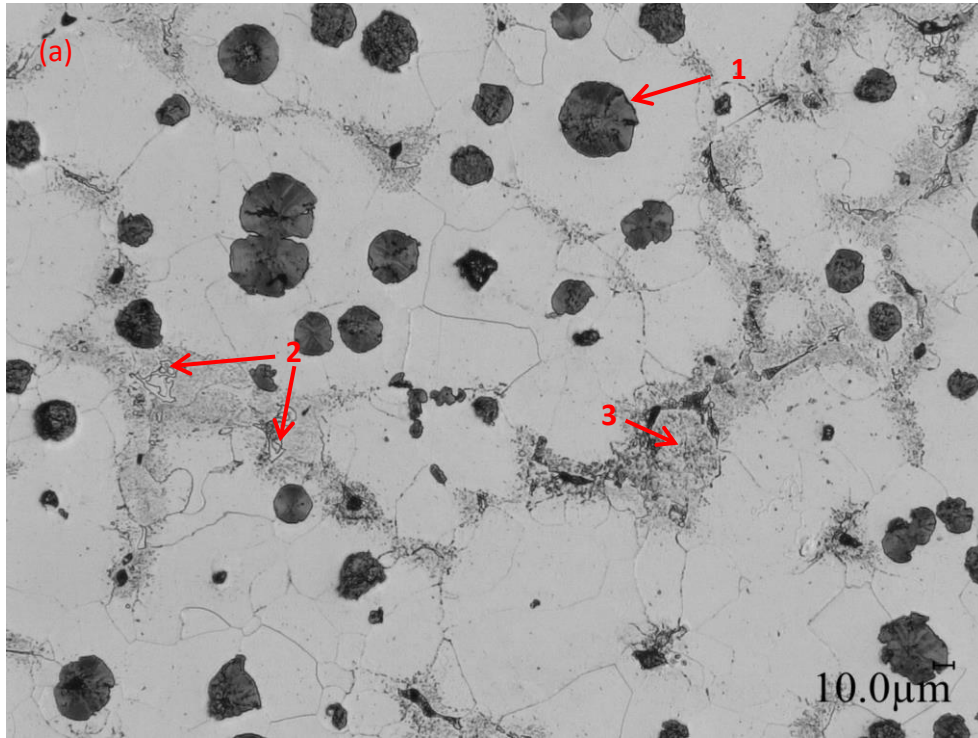


Figure 4.14 a) Non-heat-treated b) Heat-treated SiMo 5.10 (Arrows 1, 2 and 3 point to graphite particle, Mo rich phases and Primary carbides)

It can be seen from figure 4.14 a) and b) that the carbide phase and the fine precipitate phase present in grain boundary regions in the non-heat-treated SiMo 5.10 is distributed in the matrix (arrow 4) in the heat-treated SiMo 5.10 material. The annealing heat-treatment performed on the SiMo 5.10 cast iron seems to promote a uniform distribution of the Mo-rich phases in the grain boundary and matrix regions. This effect was also confirmed by [17]. Image analysis on microstructures performed by [13] showed that the amount of Mo-rich phases reduced from 7.3% to 3.2% after heat-treatment which increased the elongation. The lower average *TMF* lifetime of heat-treated SiMo 5.10 compared to its non-heat-treated equivalent (see table 4.1) can be hypothesized that the distribution and reduction of the Mo-rich phases due to heat-treatment seems to affect the *TMF* performance of SiMo 5.10 cast iron. This is supported by the fact that the graphite particle and grain sizes are similar in both materials (table 4.3). However, the effect of Mo-rich precipitate distribution on *TMF* is unclear.

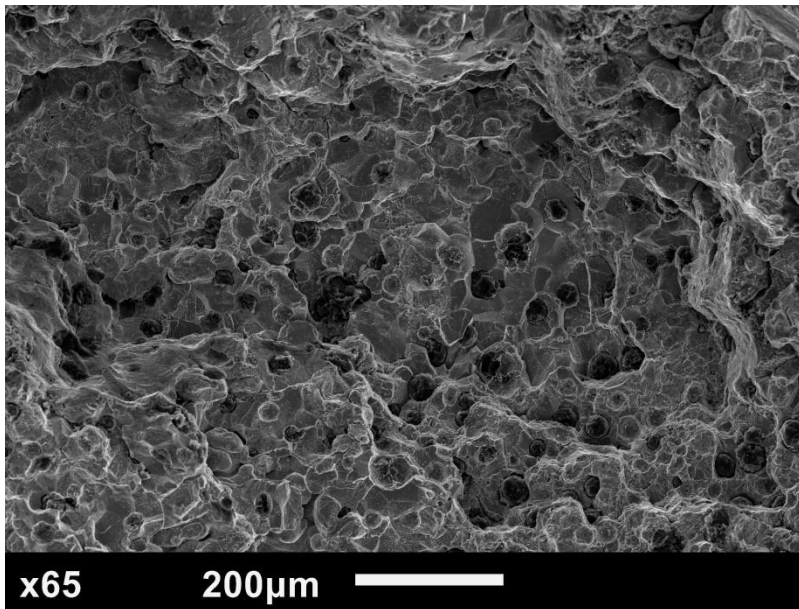


Figure 4.15 Fracture surface of SiMoNi cast iron

Figure 4.15 shows the *TMF* fracture surface morphology of SiMoNi, which exhibits river patterns and ridge. This indicates a transgranular fracture mode. Few graphite nodules appeared to be cut by the propagating crack. Some of the graphite nodules were bypassed by the crack, leaving shallow pulling-out marks, which suggests that the matrix-graphite interface still remained an effective bonding between graphite nodules and the matrix [28]. Micro and macro-hardness values of the matrix were obtained for the materials tested in this study as mentioned in section 3.7 are shown in table 4.4. The material C1 shows the highest hardness of all the materials tested and hence very brittle. This also supports the earlier discussion on fatigue vs fracture toughness

approach for C1. It can also be seen that the heat-treated SiMo 5.10 (A1 & A2) shows higher hardness than non-heat-treated SiMo 5.10 (A3). This can be explained due to the distribution of hard Mo-rich precipitates in the matrix for A1 and A2 whereas the matrix of A3 is relatively precipitate free. The micro-hardness values provide some insight on the *TMF* behavior as the fatigue crack grows through the matrix of the material.

**Table 4.4 Hardness values tested for the materials in this study**

Material	Micro-hardness (HV)	Macro-hardness (HV)
A1	272	243
A2	270	245
A3	263	260
B1	266	246
C1	335	300

# 5. Conclusions and Recommendations for Future Research

## 5.1. Conclusions

The main aim of this research was to compare the Thermo-Mechanical Fatigue (*TMF*) performance of different grades of SiMo nodular cast iron *i.e.* – SiMo 5.10, SiMo 4.05 and SiMoNi.

- It was found that SiMo 5.10 showed the best performance in the *TMF* test series 1 due to the development of relatively lower stress ranges and better stress relaxation properties at short holding time. SiMoNi and SiMo 4.05 showed the second best and third best performance respectively.
- A prolonged hold time was found to significantly reduce *TMF* lifetimes, despite similar stress and strain ranges. Average *TMF* lifetimes for SiMo 5.10 decreased by 72% whereas only by 49% in the case of SiMo 4.05 due to increase in cyclic plasticity and stress relaxation.
- While SiMo 5.10 showed better stress relaxation properties at shorter hold time, SiMo 4.05 had better stress relaxation properties at longer hold times *i.e.* the poor performance of SiMo 4.05 was not reflected at longer hold times.
- Using notched specimens of brittle materials like SiMoNi testing may not give a good representation *TMF* performance since a fracture by overloading mechanism takes over quite early in the fatigue cycle due to the presence of a notch.
- An annealing heat-treatment reduced the average *TMF* lifetimes of SiMo 5.10 by 43% despite similar stress and strain ranges compared to its non-heat-treated equivalent.
- Metallographic investigations and hardness measurements of as-cast and heat-treated materials revealed that the distribution of the Mo-rich phase from the grain boundary regions into the matrix due to the annealing heat-treatment. This seems to affect the *TMF* performance.
- By investigating the *TMF* performance and metallography samples of the two batches of SiMo 5.10 material, it can be seen that the casting process is reproducible.

## 5.2. Recommendations

- It is suggested that more tests be performed to complete the test matrix designed in this current study. This could give more insight in comparing the *TMF* performance of the SiMo nodular cast iron variants. For instance, performing long hold time tests

on non-heat-treated SiMo 5.10 and SiMoNi, the effect of stress relaxation on *TMF* performance on all the included materials can be compared.

- All the *TMF* test series in this study were conducted in 75 % partial constraint condition. This is still considered harsh in comparison to actual service conditions. The partial constraint level can be reduced by raising the  $T_{\min}$  above 50 °C or by reducing the amount of constraint,  $\gamma$  below 0.75.
- Smooth specimens of SiMoNi material is to be tested to obtain a good representation of the average *TMF* lifetimes since a notch leads the material to reach the  $K_{Ic}$  quite early in the fatigue cycle.
- Since this is a comparative study, only a single notch depth was used in all the specimens tested. By performing *TMF* tests with different notch depths, accurate  $C$  and  $m$  values can be determined for the included materials. This could provide more insights on the Paris crack growth behavior of the materials tested.
- The effect of heat-treatment on SiMo nodular cast iron variants can be studied in detail by performing the heat-treatment in the lab; and investigating the *TMF* performance and metallography samples.
- EDX analysis can identify the type of carbides to measure the reduction and distribution of the Mo-rich carbide phases from the grain boundaries due to heat-treatment.

## 6. Appendices

### A. Results of the TMF Test Series

The TMF matrix test matrix as seen in table 4.1 was constructed using individual TMF test results below:

**Table A.1 Results TMF test series 1 ( $T_{\min}$  50 °C;  $T_{\max}$  550 °C; 30s Hold time)**

Material	$\alpha$ ( $\times 10^{-6} / ^\circ\text{C}$ )	Peak Stress (MPa)	$\Delta\sigma$ (MPa)	$N_{10}$	Average $N_{10}$	SD/Avg (%)
SiMo5.1 Batch D	13.5	472	670	114	100	6.5
		474	650	108		
		473	656	100		
SiMo 5.1 Batch X	12.8	478	663	92	91	1.5
		477	665	90		
SiMo4.05	12.5	490	690	65	61	10
		490	683	65		
		492	695	54		
SiMoNi	12.8	522	740	68	85	22
		528	742	82		
		526	741	105		

**Table A.2 Results TMF test series 2 ( $T_{\min}$  150 °C;  $T_{\max}$  550 °C; 30s Hold time)**

Material	$\alpha$ ( $\times 10^{-6} / ^\circ\text{C}$ )	Peak Stress (MPa)	$\Delta\sigma$ (MPa)	$N_{10}$	Average $N_{10}$	SD/avg (%)
SiMo5.1 Batch D	13.5	438	595	88	97	12
		455	606	110		
		441	587	93		
SiMo 5.1 Batch X	13.6	444	585	105	120	32
		434	583	165		
		442	596	91		
SiMo 5.1 Non-heat Treated	13.5	446	602	246	193	24
		450	605	180		
		454	610	155		

**Table A.3 Results TMF test series 3 (T<sub>min</sub> 50 °C; T<sub>max</sub> 550 °C; 600s Hold time)**

Material	$\alpha$ ( $\times 10^{-6}$ / °C)	Peak Stress (MPa)	$\Delta\sigma$ (MPa)	N <sub>10</sub>	Average N <sub>10</sub>	SD/Avg (%)
SiMo 4.05	13.1	484	677	30	31	8.5
		483	670	34		
		484	670	29		
SiMo5.1 Batch D	13.5	498	675	23	28	2.6
		474	650	40		
		501	673	21		

## B. Previously performed *TMF* tests on SiMoNi Nodular cast iron

These *TMF* tests were performed on SiMoNi cast iron in the Mechanical Behavior Laboratory at TU Delft. All the tests were performed on notched specimens with 0.15 mm notch depth and in the temperature range 50 °C to 550 °C with a hold time of 30 s at the maximum cycle temperature 550 °C. All the tests were performed in total constraint conditions.

Material	Peak Stress (MPa)	$\Delta\sigma$ (MPa)	$N_f$
SiMoNi cast iron	572	854	5
	560	822	14
	572	864	2
	584	863	2
	573	837	13
	578	860	1
	580	865	2

## C. Measuring the Compliance of a Circumferentially Cracked dog-bone Specimen

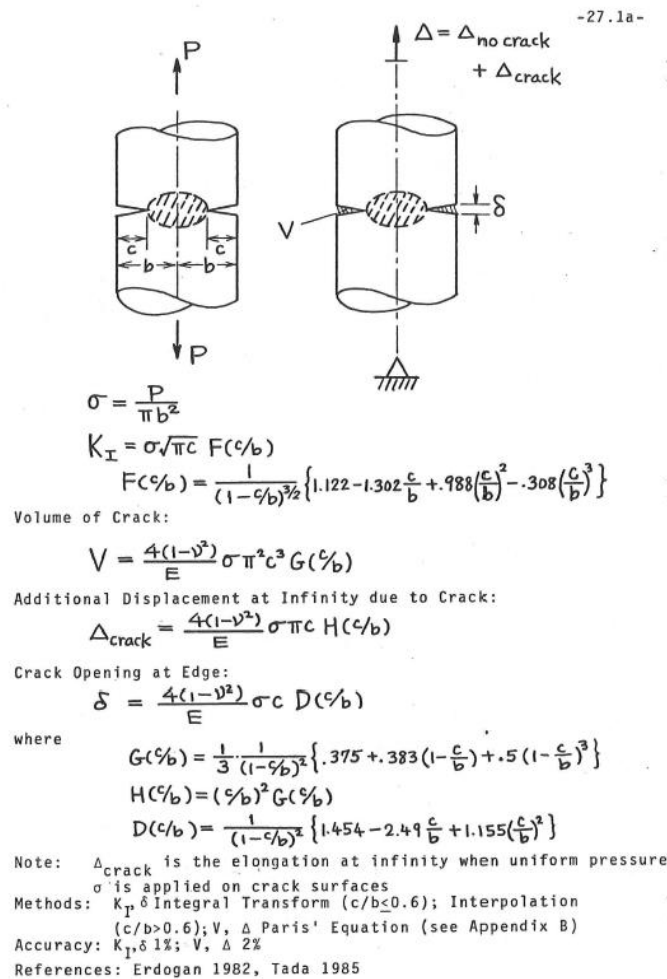


Figure C.1 Solution for measuring the compliance of circumferentially cracked specimen [38]

A cylindrical specimen with a gage length  $L_o$  and loaded in tension ( $\sigma$ ) will exhibit an elastic strain:  $\epsilon_{el.} = \sigma/E$ . The elastic elongation of the gage length is:  $\Delta L_{el.} = L_o \epsilon_{el.}$ . When a circumferential crack is introduced, the specimen will show an additional elongation (or displacement), referred to as  $\Delta_{crack}$ . Amongst other variables,  $\Delta_{crack}$  is a function of the crack length<sup>i</sup>  $c$ , as seen in figure C.1.

<sup>i</sup> However, for a certain crack length the additional displacement has a constant value throughout the material (except in the near vicinity of the crack)

Considering a gage length  $L_0$ , the total elongation of the gage length becomes:  $\Delta L_{tot.} = \Delta L_{el.} + \Delta_{crack}$ . Due to the additional displacement, the stiffness is reduced and this can be represented by an equivalent (i.e. reduced)  $E$  modulus which is given by [39]

$$E_{eq.} = \sigma / (\varepsilon_{el.} + \Delta_{crack}/L_0) \quad (C.1)$$

In this study, the increase in crack length of a same specimen of SiMoNi due to a reduction in Equivalent modulus is calculated. The initial and the final stiffness of SiMoNi specimen is measured in the elastic part of the first and final cycle hysteresis loop; for the same stress range of 200 MPa. The measured strain in the initial cycle  $1.36 \cdot 10^{-3}$ (mm/mm), is the sum of elastic strain and an additional displacement due to the presence of the notch depth, in this case  $c = 0.15$  mm. The  $\Delta_{crack}$  is calculated for the initial cycle using the Tada solution [38] as  $2.14 \cdot 10^{-6}$  mm; from which the elastic strain in the initial cycle is calculated as  $1.359 \cdot 10^{-3}$  (mm/mm), which is constant throughout the test. Thus, the measured strain in the final cycle,  $1.63 \cdot 10^{-3}$ (mm/mm) is the sum of a known elastic strain and unknown displacement due to the final crack length,  $c$ . Substituting these value in the Tada solution for  $\Delta_{crack}$ , a polynomial of degree 6 is obtained:  $0.002c^6 - 0.019c^5 - 0.09c^3 + 0.47c^2 - 0.72c + 0.25 = 0$ , of which one of the roots give the value of final crack length,  $c = 0.486$  mm.

## D. MATLAB scripts

### **For calculating TMF lifetime**

```
%Program to calculate Paris Crack growth%
a=[];
a=0.15:0.01:1.20; %crack growth%
K=[];
C=1.5*10^-10; %Paris Parameters%
m=3.6;
S=444; %Peak stress%
for i=1:106
    Y(i)=(1/(1-a(i)*10^-3/0.003)^(3/2))*(1.122-
1.302*(a(i)*10^-3/0.003)+0.988*(a(i)*10^-3/0.003)^2-
0.308*(a(i)*10^-3/0.003)^3);

    K(i)=S*sqrt(3.14*a(i)*10^-3)*Y(i);
end
dN=[];
for i=1:105
    dN(i)=((a(i+1)*10^-3)-(a(i)*10^-3))/((K(i)^m)*(C));
    N10=sum(dN); %lifetime%
end
```

### **For calculating the final crack length in SiMoNi**

```
%Script to calculate final crack length in SiMoNi%
a=0.15; %initial crack length%
C=3.3*10^-11; %paris Parameters
m=3.58;
S=742; %stress range%
N=82; %N10%

Y=(1/(1-a*10^-3/0.003)^(3/2))*(1.122-1.302*(a*10^-
3/0.003)+0.988*(a*10^-3/0.003)^2-0.308*(a*10^-3/0.003)^3);

K=S*sqrt(3.14*a*10^-3)*Y;

Cg=C*(K)^m; %crack growth per cycle%

CG=N*Cg; %final crack length%
```

**For calculating the  $\Delta_{crack}$  in SiMoNi cast iron**

`%Delta Crack in Tada solution for the first cycle%`

`a=0.15;`

`G=(1/3) * (1/(1-a*10^-3/0.003)^2) * (0.375+0.383*(1-(a*10^-3/0.003))+0.5*(1-(a*10^-3/0.003))^3);`

`H=((a*10^-3/0.003)^2)*G;`

`DelC=((4*(1-0.33^2))/168534)*56*pi*(a*10^-3)*H;`

# Acknowledgements

I would like to first thank my initial supervisor at TU Delft, Dr. Ir. Michael Janssen for introducing me to the topic of Thermo-Mechanical Fatigue and also this current thesis project. His door was always open for me whenever I had a question about my research or other aspects. His consistent inputs on my research gave me a good understanding of the subject.

I also extend my gratitude to Prof. Dr. Ir. Leo Kestens for agreeing to be my supervisor and chair of the graduation committee. His speedy efforts enabled me to graduate on time.

I would like to deeply thank Dr. Ir. Ton Riemsdag, for his constant motivation and efforts to review my work. He taught me the nuances in performing research which enabled me to become a better researcher. Thank you Ton for your constant moral support during tough times!

Many thanks to Ir. Elise Reinton for introducing me to the test set-up and her constant guidance in the experimental aspects of this project.

This project would not have been possible without DAF trucks N.V. I would like to thank Mark Van Drogen, Aakarshit Kalra, Paul Steuten and Reinhard Uebel for the constant support and providing inputs during the constructive discussions of the results at DAF trucks location.

Finally, I must express my sincere gratitude to my parents and to my friends for providing me with continuous encouragement throughout study and through the process of researching and writing this thesis. This accomplishment would not have been possible without them. Thank you all!

## 7. Bibliography

- [1] S. International, "Surface Vehicle Standard - High temperature Materials for Exhaust Manifolds J2515," December 2017.
- [2] J. Pan, K. Avery and C. Engler-Pinto, "Effect of Temperature Cycle on Thermomechanical Fatigue Life of a High Silicon Molybdenum Ductile Cast Iron," *SAE International*, 2015.
- [3] Y. Yun-long, C. Zhan-yi, L. Zhen-song and Y. Hai-xia, "Thermal Fatigue Behaviour and Cracking Characteristics of High Si-Mo Nodular Cast Iron for Exhaust Manifolds," *Journal of Iron and Steel Research*, vol. 20, no. 6, pp. 52-57, 2013.
- [4] A. Kalra, "Thermo-Mechanical Fatigue-Lifetime Determination of Diesel Engine Exhaust Manifolds, Master Thesis," TU Delft, Delft, 2016.
- [5] "Material Data Sheet GJS SiMoNi5-1-1," GF Automotive, 2017.
- [6] K. Papis, S. Tunzini and W. Menk, "Cast iron alloys for exhaust applications," in *10th International Symposium on the Science and Processing of Cast Iron – SPCI10*, Mar Del Plata, Argentina, 2014.
- [7] FVV, "TMF Lebensdauerberechnung ATL-Heisteile," FVV, Frankfurt, 2010.
- [8] H. Sehitoglu, "Thermal and Thermomechanical Fatigue of Structural Alloys," in *ASM Handbook Online*, ASM International, 2003.
- [9] C. F. Walton and T. J. Opar, in *Iron Castings Handbook*, Iron Castings Society, Inc., 1981, pp. 121-122.
- [10] N. Verkleij, "SiMo ductile irons for the application of exhaust manifolds and turbo charger housings: A literature survey," Delft University of Technology and DAF Trucks N.V., Delft, 2010.
- [11] X. Wu, G. Quan, R. Macneil, Z. Zhang, X. Liu and C. Sloss, "Thermomechanical Fatigue of Ductile Cast Iron and its Life Prediction," *Metallurgical and Materials Transactions A*, vol. 46A, pp. 2530-2542, 2015.
- [12] M. Ekstrom and S. Johnson, "High-Temperature Mechanical and Fatigue Properties

- of Cast alloys intended for use in Exhaust Manifolds," *Materials Science and Engineering A*, vol. 616, pp. 78-87, 2014.
- [13] D. Li, R. Perrin, G. Burger, D. McFarlan, B. Black, R. Logan and R. Williams, "Solidification Behavior, Microstructure, Mechanical Properties, Hot Oxidation and Thermal Fatigue Resistance of High Silicon SiMo Nodular Cast Irons," *SAE International*, 2004.
- [14] L. M. berg and C. Hartung, "Solidification of SiMo Nodular Cast Iron for High Temperature Applications," *Trans Indian Institute of Metals*, vol. 65(6), p. 633–636, 2012.
- [15] C. Labrecque and M. Gagne, "Ductile Iron Fifty Years Of Continuous Development," *Canadian Metallurgical Quarterly*, vol. 37, no. 5, pp. 343-378, 1998.
- [16] Y.-J. Kim and H. J. Y.-J. Oh, "High Temperature Low-Cycle Fatigue Property of Heat-Resistant Ductile-Cast Irons," *Metallurgical and Materials Transactions A*, vol. 40A, pp. 2087-2097, 2009.
- [17] D. Li and C. Sloss, "Heat treatment of heat resistant cast alloys," *International Journal of Metalcasting*, vol. 9, no. 2, pp. 6-20, 2015.
- [18] R. L. Colombo and L. Bonello, "Relationships Between Fatigue Resistance and Spheroidization of Graphite in Nodular Cast Iron," *Metallurgy*, vol. 16, pp. 327-330, 1983.
- [19] S. Dawson and T. Schroeder, "Compacted Graphite Iron: A Viable Alternative," *Engineered Casting Solutions AFS*, 2000.
- [20] S. Ghodrati, "Thermo-mechanical Fatigue of Compacted Graphite Iron in Diesel Engine Components, PhD. Thesis," TU Delft , Delft , 2013 .
- [21] B. Black, G. Burger, R. Logan and R. Perrin, "Microstructure and Dimensional Stability in Si-Mo Ductile Irons for Elevated Temperature Applications," in *International Body Engineering Conference & Exhibition*, Paris, France, 2002.
- [22] A. Alhoussein, M. Risbet, A. Bastien, J. Chobaut, D. Balloy and J. Favergeon, "Influence of silicon and addition elements on the mechanical behavior of Ferritic Ductile Cast Iron," *Materials Science & Engineering A*, vol. 605, p. 222–228, 2014.
- [23] T. S. Lui and C. G. Chao, "High-temperature properties of ferritic spheroidal

- graphite cast iron," *Journal of Material Science* , vol. 24, p. 2503-2507, 1989.
- [24] R. González-Martínez, U. d. I. Torrea, A. Ebelb, J. Lacazeb and J. Sertuchaa, "Effects of high silicon contents on graphite morphology and room temperature mechanical properties of as-cast ferritic ductile cast irons," *Materials Science & Engineering A* , vol. 712, p. 803–811, 2018.
- [25] Foundry Handbooks, Vol. 1: Cast Irons, Beijing: Mechanical Engineering Publisher, 2002.
- [26] C. Halászi, C. Gaier and H. Dannbauer, "Fatigue Life Prediction Of Thermo-Mechanically Loaded Engine Components," *European Automotive Engineers Cooperation*, vol. 07, 2007.
- [27] N. Zafeiropoulos, "Failure mechanisms of SiMo ductile iron at high temperature A diesel engine exhaust manifold application, MSc thesis," TU Delft, Delft , 2014.
- [28] X. Wu, G. Quan, R. Macneil and Z. Zhang, "Failure Mechanisms and Damage Model of Ductile Cast iron under Low-Cycle Fatigue Conditions," *Metallurgical and Materials Transaction A*, vol. 45A, pp. 5085-5097, 2014.
- [29] Y.-J. Kim, H. Jang and Y.-J. Oh, "High-Temperature Low-Cycle Fatigue Property of Heat-Resistant Ductile-Cast Irons," *Metallurgical and Materials Transactions A* , vol. 40A, pp. 2087-2097, 2009.
- [30] P. Matteis, G. Scavino, A. Castello and D. Firrao, "High Temperature Fatigue Properties of a SiMo Ductile Cast Iron," *Procedia Materials Science* , vol. 3 , pp. 2154-2159, 2014.
- [31] X. Liu, G. Quan, X. Wu, Z. Zhang and C. Sloss, "Simulation of Thermomechanical Fatigue of Ductile Cast Iron and Lifetime Calculation," *SAE International* , vol. 01, no. 0552, 2015.
- [32] M. Janssen, *Materials at high temperature: Mechanical behaviour of materials at high temperature*, Powerpoint, Delft: TU Delft, 2017.
- [33] D. t. N.V., "Standard - Nodular Cast Iron, Alloyed," 2010.
- [34] S. Brookes, A. Scholz, H. Klingelhöffer, M. Whittaker, M. Loveday, A. Scholz, A. Wisby, N. Ryder, R. Lohr and S. Stekovic, "Code of Practice For Force-Controlled Thermo-Mechanical Fatigue Testing," 2015.

- [35] ASTM International Standard, "Standard practice for strain controlled thermomechanical fatigue testing, E 2368 – 10," 2010.
- [36] S. Ghodrati, A. Reimslag, M. Janssen, J. Sietsma and L. Kestens, "Measurement and characterization of thermo-mechanical fatigue in compacted graphite iron," *International Journal of Fatigue*, vol. 48, pp. 319-329, 2013.
- [37] T. Opraus, "Determining the Suitability and Application of CNT Test Specimens for Failure Assessment of Welded High Strength Steels," TU Delft, Delft, 2016.
- [38] H. Tada, P. C. Paris and G. R. Irwin, *Stress Analysis of Cracks Handbook*, New York: ASME press, 2000.
- [39] A. Reimslag, *Compliance Cracked Specimen*, Delft.
- [40] I. Hervas, A. Thuault and E. Hug, "Damage Analysis of a Ferritic SiMo Ductile Cast Iron Submitted to Tension and Compression Loadings in Temperature," *Metals*, vol. 5, pp. 2351-2369, 2015.
- [41] M. Ekström, "Development Of A Ferritic Ductile Cast Iron For Increased Life In Exhaust Applications; Licentiate Thesis," KTH Royal Institute of Technology, Stockholm, Sweden, 2013.